Oncogene-induced matrix reorganization controls CD8$^+$ T cell function in the tumor microenvironment

Hawley C. Pruitt[1,2†], Ashley M. Fuller[3,4,5,11,12†], Hoogeun Song[3,4,5,11,12], Ying Liu[3,4,5,11,12], Ann DeVine[3,4,5,11,12], Rohan Katti[3,4,5,11,12], Samir Devalaraja[3,4,5,11,12], Gabrielle E. Ciotti[3,4,5,11,12], Michael Gonzalez[10], Erik F. Williams[6,7,8,11,12], Ileana Murazzi[12], Nicolas Skuli[5,11,12], Hakon Hakonarson[10] , Kristy Weber[4,9,11,12], Malay Haldar[3,4,5,11,12], Joseph A. Fraietta[6,7,8,11,12, ‡], Sharon Gerecht[1,13, ‡], T. S. Karin Eisinger-Mathason[3,4,5,11,12, ‡, *]

Affiliations

[1]Johns Hopkins Physical Sciences–Oncology Center

[2]Department of Chemical and Biomolecular Engineering and Institute for NanoBioTechnology, Department of Materials Science and Engineering, Department of Oncology, Johns Hopkins University, Baltimore, MD

[3]Department of Pathology & Laboratory Medicine.

[4]Penn Sarcoma Program.

[5]Abramson Family Cancer Research Institute.

[6]Department of Microbiology.

[7]Center for Cellular Immunotherapies.

[8]Parker Institute for Cancer Immunotherapy.

[9]Department of Orthopedic Surgery.

[10]Children's Hospital of Philadelphia

[11]Perelman School of Medicine.

[12]University of Pennsylvania, Philadelphia, PA, USA.

[13] Duke University, Durham, NC, USA.

[†]authors contributed equally

[‡]co-corresponding authors

***Correspondence should be addressed to:** T.S. Karin Eisinger-Mathason, Abramson Family Cancer Research Institute, University of Pennsylvania, 414 BRB II/III, 421 Curie Boulevard, Philadelphia, PA 19104-6160. Phone: 215-898-9086; Fax: 215-746-5511; E-mail: karineis@pennmedicine.upenn.edu

ABSTRACT

$CD8^+$ T cell dysfunction is a critical barrier to anti-tumor immunity, but molecular mechanisms underlying the regulation of T cell dysfunction in solid tumors are diverse and complex. Extracellular matrix (ECM) composition facilitates solid tumor progression in part by inhibiting T cell migration/infiltration; however, the impact of individual ECM molecules on T cell function in the tumor microenvironment (TME) is virtually unknown. Moreover, upstream regulators of aberrant ECM deposition/organization in solid tumors are poorly defined. Therefore, we investigated the regulation and effects of ECM composition on $CD8^+$ T cell function in undifferentiated pleomorphic sarcoma (UPS). This immunologically "hot" soft-tissue sarcoma exhibits durable responses to checkpoint therapy in some human patients, suggesting it may provide insights into strategies for optimizing T cell function and improving immunotherapy efficacy. Using an autochthonous model of UPS and data from multiple human patient cohorts, we discovered a multi-pronged mechanism wherein oncogene-induced remodeling of the TME promotes $CD8^+$ T cell dysfunction, suppresses T cell-mediated cytolysis, and enhances immune evasion. Specifically, we observed that the transcriptional co-activator Yap1, which we previously linked to UPS progression, promotes the aberrant deposition of collagen VI in the UPS TME. In turn, collagen VI induces $CD8^+$ T cell dysfunction by inhibiting T cell autophagic flux and remodeling fibrillar collagen architecture in the TME. Furthermore, collagen type I opposed ColVI in this setting, acting as tumor suppressor. Thus, our findings reveal that $CD8^+$ T cell-mediated anti-tumor immunity in solid cancers is dependent upon oncogene-mediated ECM composition and remodeling in the TME.

INTRODUCTION

Immunosuppression in the solid tumor microenvironment (TME) is a barrier to T cell-mediated anti-tumor immunity. Tumors evade host adaptive immune responses via induction of $CD8^+$ T cell dysfunction, a hypofunctional state characterized by overexpression of inhibitory cell-surface receptors (e.g., PD-1, TIM3, LAG3), reduced effector function, and impaired proliferative capacity [1,2]. Molecular mechanisms underlying $CD8^+$ T cell dysfunction in solid cancers are of significant interest due to their impact on immunotherapy strategies. However, most prior studies in this area have focused on the roles of continuous antigen exposure/repetitive T cell receptor stimulation, immune checkpoint-mediated inhibitory signaling, and immunosuppressive cytokines [2,3]. Moreover, the importance of TME contexture in the setting of T cell-based

therapies is poorly described. Thus, a more comprehensive and physiological evaluation of $CD8^+$ T cell dysfunction in solid tumors is critical for improving our understanding of immune evasion mechanisms in the TME and advancing actionable interventions.

Soft tissue sarcoma (STS) is a heterogeneous group of solid mesenchymal malignancies comprised of ~70 distinct histologic tumor subtypes [4-6]. Consistent with their mesenchymal origins, STS are characterized by mesenchymal gene expression, extensive secretion of extracellular matrix (ECM) components, and increased ECM stiffness relative to normal tissues [7-10]. Interestingly, these features are also observed in high-grade, poorly differentiated epithelial tumors where they are linked to progression, therapeutic resistance, and poor clinical outcomes [7,11-22]. Recent studies have shown that the ECM facilitates cancer progression in part by inhibiting T cell migration/infiltration [23-26]. However, the roles of individual ECM proteins in this process remain unclear. Moreover, very little research has addressed the effects of ECM molecules on T cell function, or identified upstream regulators of aberrant ECM deposition and composition/organization in solid tumors. The paucity of available data pertaining to these relationships indicates that further study, particularly *in vivo*, is necessary.

Members of the collagen superfamily, of which there are nearly 30 distinct molecular species, are some of the most abundant and diverse ECM constituents in both normal tissues and solid tumors [27]. Although the roles of specific collagen species in cancer-associated processes are still under investigation, a growing body of literature indicates that individual collagen molecules can have context-specific functions in the TME. For example, type I collagen (ColI), a fibrillar collagen that forms prototypical collagen fibers, promotes or is associated with malignant progression in some tumor settings [28,29], but shows protective effects in others [30-32]. These findings underscore the need to systematically interrogate the roles of individual collagen molecules, particularly with respect to their potential impacts on adaptive immunity, in specific tumor contexts.

Undifferentiated pleomorphic sarcoma (UPS) is a relatively common STS subtype that predominantly arises in adult skeletal muscle and has a 10-year survival rate of only ~25% [5,33]. Although STS are generally considered immunologically “cold”, recent clinical studies have revealed that patients with UPS can exhibit objective clinical responses to immune checkpoint inhibition [34-37]. These encouraging findings suggest that studies of UPS may provide valuable insights into strategies by which to ameliorate T cell function and responses to immunotherapy in solid tumors. Our previous work linked the intrinsic oncogenic functions of the

transcriptional co-regulator Yes-associated protein 1 (YAP1), the central Hippo pathway effector, to UPS cell proliferation and tumor growth via downstream effects on NF-κB [38-41]. However, we had not investigated the contribution of the Yap1-NF-κB axis to the broader UPS microenvironment or immune cell activity. In some epithelial tumors, cancer cell-intrinsic Yap1 has been shown to modulate recruitment and differentiation of macrophages and myeloid-derived suppressor cells, suggesting a role in modulation of infiltrating immune cells [42-44]. However, this observation has not been confirmed in mesenchymal cancers. Importantly, YAP1 possesses mechanosensory functions, and its nuclear localization and activity increase in response to stiff environments such as those found in tumor tissue [45]. Therefore, in this study, we interrogated the role of UPS cell-intrinsic Yap1 signaling in ECM deposition/organization and adaptive immune cell function in the TME. We discovered a novel role for Yap1 in the regulation of ECM composition and cytotoxic T cell function, and found that collagen type VI (ColVI), a non-fibrillar collagen, indirectly modulates effector T cell function by remodeling ColI. We further identify ColVI as a putative ECM-associated biomarker of diagnosis and survival in human UPS. Our findings implicate YAP1 inhibition, in combination with immunotherapy, as a promising approach to mitigate immune evasion mechanisms in the TME of patients with solid tumors.

RESULTS

UPS cell-intrinsic Yap1 inhibits T cell activation and promotes CD8$^+$ T cell dysfunction

Using the genetically engineered mouse model (GEMM) of skeletal muscle-derived UPS, *Kras*$^{G12D/+}$; *Trp53*$^{fl/fl}$ (KP) [46,47], we previously showed that Yap1 promotes UPS tumorigenesis and progression via activation of sarcoma cell-intrinsic NF-κB. In this GEMM system, tumors are generated by injection of adenovirus expressing Cre recombinase into the gastrocnemius muscle. Recombination initiates oncogenic *Kras* expression and deletes floxed alleles in infected muscle progenitor cells [46,47]. *TP53* mutation and deletion are prevalent in human UPS [48], as is hyperactivation of the MAPK pathway, which occurs downstream of KRAS activation [49]. We observed reduced tumor formation when we introduced *Yap1*$^{fl/fl}$ or *Rela*$^{fl/fl}$ (p65 NF-κB) alleles into the KP GEMM, creating *LSL-Kras*$^{G12D/+}$; *Trp53*$^{fl/fl}$; *Yap1*$^{fl/fl}$ (KPY; [39]) and *Kras*$^{G12D/+}$; *Trp53*$^{fl/fl}$; *Rela*$^{fl/fl}$ (KPR) animals, respectively (**Fig. 1A, B**). Restoration of NF-κB signaling in *Yap1*-deficient tumors (KPY) via introduction of constitutively active *Ikk2* alleles (*LSL-Kras*$^{G12D/+}$; *Trp53*$^{fl/fl}$; *Yap1*$^{fl/fl}$; *Ikk2*$^{CA/CA}$; KPYI) rescued

tumor formation and latency, supporting the conclusion that NF-κB is activated downstream of Yap1 and can rescue Yap1 deficiency *in vivo.*

In addition to its role in Yap1-mediated sarcomagenesis [39], NF-κB has many well-established Yap1-independent effects on inflammation and tumor progression [50]. Therefore, although the ability of the KPYI model to rescue Yap1-dependent tumor latency and growth was of great interest to our group, a caveat of this model is that constitutively active *Ikk2* expression may also exert confounding Yap1-independent effects on tumor intrinsic and microenvironmental factors. As a result, we concentrated our efforts on elucidating upstream mechanisms by which Yap1, specifically, impacts the UPS TME. First, to ascertain the functional consequences of UPS cell-intrinsic Yap1 signaling on the TME, we performed microarray-based gene expression analysis comparing 5 unique KP and KPY bulk tumors. Loss of *Yap1* enhanced expression of numerous pathways associated with immune activation, suggesting that UPS cell-intrinsic Yap1 contributes to immunosuppression through an unknown mechanism (**Fig. 1C**). To investigate how Yap1 controls immunosuppression in UPS, we performed flow cytometric and automated immunohistochemical (IHC) analysis of KP and KPY tumors. We did not detect changes in myeloid cell (dendritic cells, macrophages, neutrophils) infiltration or polarization, nor did we observe differences in B cell content (**Supp. Fig. 1A-C**). However, we did observe increased proportions of $CD44^{hi}$ $CD8^+$ and $CD4^+$ T cells in KPY relative to KP tumors, indicative of enhanced T cell activation (**Fig. 1D, E**). Furthermore, the percentage of dysfunctional effector $CD8^+$ T cells ($CD39^+/Pd1^+$ and $Tim3^+/Pd1^+$ $CD8^+$ T cells) was higher in KP tumors compared to KPY (**Fig. 1F, G**). Markers associated with central $CD8^+$ memory T cell differentiation (CD62L, CD127) remained unchanged (**Supp. Fig. 2A**). Importantly, in KPY mice, the observed increases in T cell activation could not be attributed to reduced immunosuppressive $Foxp3^+$ T regulatory cell content, nor to enhanced effector T cell infiltration (**Supp. Fig. 1B-C**). In fact, $CD4^+$ and $CD8^+$ T cell content was modestly decreased in KPY relative to KP tumors. Therefore, we conclude that Yap1 may promote $CD8^+$ T cell dysfunction but likely does not impact T cell recruitment to the TME.

To explore the relationship between $Yap1^+$ UPS cells and T cell activation in more detail, we evaluated the expression of the T cell cytolysis marker, granzyme B (*Gzmb*) [51], in GEMM tumors by qRT-PCR (**Fig. 1H**). *Gzmb* expression (normalized to total T cells; *Cd3e*) was significantly increased in KPY tumors, providing further evidence that $Yap1^+$ UPS cells are associated with immunosuppression. Therefore, we determined if

tumor cell-intrinsic Yap1 modulates T cell effector function in addition to inhibitory surface marker expression. To this end, we treated tumor-bearing KP and KPY mice with αPd-1 checkpoint therapy or isotype control antibody. We hypothesized that immune checkpoint blockade would show increased efficacy in KPY animals due to enhanced T cell activation, but have no effect in KP mice. Consistent with this hypothesis, time to maximum tumor volume was significantly increased in KPY, but not KP, animals (**Fig. 1I**). Notably, one KPY mouse experienced complete and lasting tumor regression. We further evaluated the effect of YAP1$^+$ UPS cells on T cell function by leveraging human chimeric antigen receptor T (CART) cells that target the Tn glycoform of mucin 1 on human tumor cells (TnMUC1 CART cells [52]). This antigen is expressed on human STS-109 cells, derived from a UPS patient tumor (**Supp. Fig. 2B**). We co-cultured TnMUC1-CART cells with STS-109 cells expressing control or *YAP1*-specific shRNAs (shYAP1) at various effector:target ratios and analyzed longitudinal cytolysis (**Fig. 1J**). In this experiment, we observed that loss of *YAP1* expression in UPS cells enhances cytotoxic T cell function, confirming that YAP1$^+$ UPS cells promote immunosuppression. To explore this data in the context of human patient samples, we leveraged The Cancer Genome Atlas (TGCA) Sarcoma dataset [48]. Consistent with our experimental findings, markers of T cell activation (*GZMB* and perforin; *PRF1*) in human UPS tumors correlate with improved overall, disease-specific, and disease-free survival in these patients (**Fig. 1K, L**; **Supp. Fig. 2C**). Furthermore, *GZMB* and *PRF1* gene expression negatively correlate with *YAP1* levels in these tumors (**Fig. 1M, N**). Thus, although sarcomas are generally considered immunologically “cold”, these data suggest that cytotoxic T cell activation is a critical factor in UPS patient survival, and that modulating Yap1 and T cell activity may improve clinical outcomes.

UPS cell-intrinsic Yap1 promotes collagen VI deposition in the TME

We next sought to define the mechanism of crosstalk between Yap1$^+$ tumor cells and infiltrating T cells, reasoning that soluble mediators might regulate these communication patterns. To test this hypothesis, we co-cultured control and *YAP1*-deficient STS-109 human UPS cells with TnMUC1 CAR T cells and measured 31 cytokines and chemokines in the resulting supernatants. Many analytes could not be detected in these co-cultures; those that did surpass the lower limit of detection were generally stable in the presence or absence of UPS cell-intrinsic *YAP1* (**Supp. Fig. 3A**, **Supplemental Table 1**). UPS cells co-cultured with normal human donor T cells (ND T cells) gave similar results (**Supp. Fig. 3B**), indicating that soluble factors are likely not

major contributors to UPS cell-T cell crosstalk. These findings support the conclusion that YAP1 may control $CD8^+$ T cell function in the TME through non-soluble factors.

YAP1 has mechanosensing properties associated with ECM remodeling [53]. Therefore, we investigated whether these processes, rather than soluble signaling molecules, are required for YAP1-mediated T cell suppression in the UPS TME. Using our microarray analysis of KP and KPY tumors to identify Yap1-dependent matrix genes, we found that many pathways associated with ECM remodeling, including muscle and blood vessel development pathways, are altered in KPY tumors relative to KP (**Supp. Fig. 3C**). We also observed that genes encoding many members of the collagen superfamily, particularly collagen type VI (ColVI), were substantially downregulated in KPY relative to KP tumors (**Fig. 2A**, **Supp. Fig. 3D-F**). Multiple genes encode ColVI (e.g., *Col6a1*, *Col6a2*, *Col6a3*), each of which results in a unique protein chain. *Col6a1* is indispensable for ColVI protein expression [54]. IHC analysis of bulk tumor sections revealed that ColVI expression in the TME was heterogeneous (**Supp. Fig 3G**), potentially due to secretion by multiple cell types [55]. However, we did find examples wherein ColVI deposition was strikingly reduced in KPY tumors compared to KP (**Fig. 2B**). Therefore, we validated these findings *in vitro* by qRT-PCR and Western blotting in UPS cell lines derived from the KP GEMM (KP cells). Specifically, KP cells transduced with one of multiple *Yap1*-specific shRNAs expressed substantially less *Col6a1* and *Col6a2* than control cells; *Col6a3* was more modestly reduced (**Fig. 2C, D**). In contrast, we could not validate a role for Yap1 in the regulation of collagen type III expression (**Supp. Fig. 3H**), indicating the potential specificity of this regulation.

To confirm the relationship between Yap1 and ColVI in UPS, we treated tumor-bearing KP mice, as well as KP cells *in vitro*, with a combination of the histone deacetylase inhibitor Vorinostat (also known as Suberoylanilide Hydroxamic Acid; SAHA) and the BRD4 inhibitor JQ1 or vehicle control. We have previously reported that SAHA/JQ1 treatment inhibits Yap1 expression in UPS cells [39]. Microarray, IHC, western blotting, and qRT-PCR analyses confirmed that ColVI gene and protein expression were substantially downregulated in SAHA/JQ1-treated cells and tumors (**Fig. 2E-G, Supp. Fig. 3J**). Taken together, these data suggest that UPS-cell intrinsic Yap1 promotes the aberrant deposition of ColVI in the TME, and that genetic and pharmacologic inhibition of Yap1 can reverse this process.

Yap1-mediated ColVI deposition promotes $CD8^+$ T cell dysfunction

Based on our findings, we hypothesized that Yap1-mediated ColVI deposition in the UPS ECM enhances T cell inhibitory marker expression and dysfunction. To test this idea, we developed a novel system wherein control and *Yap1*-deficient KP cells were stimulated to deposit ECM, which was then decellularized and incubated with activated $CD8^+$ T cells (decellularized ECM, dECM; **Fig. 2H**). We targeted *Col6a1* in this assay because *Col6a1*-deficient cells cannot synthesize ColVI protein [54]. Immunofluorescent staining revealed that KP cells deposit substantial amounts of ColVI, whereas *Yap1*-deficient cells do not, confirming the regulatory role of UPS cell-intrinsic Yap1 in ColVI secretion (**Fig. 2I**). Moreover, compared to $CD8^+$ T cells cultured on dECM from *Yap1*-deficient KP cells, $CD8^+$ T cells incubated on KP dECM (containing high levels of Yap1 and ColVI) expressed significantly higher levels of the T cell inhibitory receptors Pd-1 and Tim-3 (**Fig. 2J**). These results support our earlier findings (**Fig. 1F-G**) that UPS cell-intrinsic Yap1 promotes $CD8^+$ T cell dysfunction. We then determined the specific effects of ColVI, downstream of Yap1, on $CD8^+$ T cell surface marker expression by generating dECM from ColVI-deficient KP cells. Compared to matrix from control cells, dECM from shCol6a1 KP cells significantly reduced $CD8^+$ T cell dysfunction as measured by dual expression of Pd-1 and Tim-3 (**Fig. 3A, B**). We also compared dECM from wildtype and *Col6a1*$^{-/-}$ mouse embryonic fibroblasts (MEFs) and observed no differential effects on T cell inhibitory receptor expression, indicating that sarcoma cell-derived ECM exhibits more immunosuppressive characteristics (**Fig. 3C, D**). Consistent with this observation, ColVI deposition was strikingly enhanced in control sarcoma-derived ECM compared to WT MEF-derived ECM, suggesting that untransformed fibroblasts do not produce sufficient ColVI to promote T cell dysfunction (**Fig. 3A, C**). To test the effects of COLVI on T cell function, we employed the human CART-TnMUC1 system [52]. We analyzed longitudinal cytolysis of STS-109 UPS cells expressing control or *COL6A1*-specific shRNAs. We observed that loss of *COL6A1* expression enhances cytotoxic T cell function, phenocopying the effects of *YAP1* depletion (**Fig. 3E, F**). Moreover, we determined that ColVI is actively secreted by UPS cells into culture medium (**Supp. Fig. 4A**), where it can suppress CART-TnMUC1-mediated cytolysis and promote T cell dysfunction.

In light of our *in vitro* findings that ColVI suppresses $CD8^+$ T cell function, we next investigated the effect of ColVI on T cell function *in vivo*. First, we determined that ColVI depletion does not affect KP tumor-derived cell proliferation *in vitro* (**Supp. Fig. 4B, C**). This finding is consistent with the hypothesis that the dominant role of ColVI is specific to immune modulation in the TME. We pursued these findings *in vivo* by

generating control and *Col6a1* shRNA-expressing UPS tumors (syngeneic allograft) in C57BL/6 hosts. In these immunocompetent mice, ColVI-deficient tumors were significantly smaller and slower growing than control tumors (**Fig. 3G-H**). We demonstrated that ColVI-dependent tumor growth is mediated by T cell inactivation by depleting $CD8^+$ T cells in the syngeneic transplant system (**Supp. Fig. 4D**); control and shCol6a1 tumors grew at the same rate in this setting (**Fig. 3I**). We also generated orthotopic tumors by injecting control and shCol6a1-expressing KP cells into the gastrocnemius muscles of immunocompetent C57BL/6 mice (**Fig. 3J**, **Supp. Fig. 4E**). Flow cytometric analysis indicated that the proportion of $CD8^+$ T cells expressing markers of T cell dysfunction, including TOX, TIM-3, CD39, and LAG3, was significantly decreased in ColVI-deficient compared to control tumors (**Fig. 3K, L**). Taken together, these findings confirm that Yap1-mediated ColVI deposition in the UPS TME promotes $CD8^+$ T cell dysfunction and immune evasion.

ColVI indirectly promotes $CD8^+$ T cell dysfunction by remodeling collagen I

Next, we explored the mechanism by which ColVI in the UPS TME promotes $CD8^+$ T cell dysfunction. We first asked whether $CD8^+$ T cell dysfunction is induced following direct interaction with secreted ColVI via known ColVI receptors. To test this hypothesis, we cultured activated human $CD8^+$ T cells on ColVI-containing hydrogels and inhibited or blocked ITGB1, NG2 (CSPG4), CMG2 and ITGAV (**Supp. Fig 5A-D**). Neutralization of ITGB1 or NG2 with blocking antibodies had no effect on $CD8^+$ T cell dysfunction as measured by dual expression of TIM3 and PD1, nor did it rescue loss of Ki67+ cells seen in ColVI hydrogels. Similar results were obtained following treatment of human $CD8^+$ T cells with cilengitide, a selective inhibitor of $\alpha v\beta 3$ and $\alpha v\beta 5$ integrins [56], and with activated CD8+ T cells from *Cmg2*$^{-/-}$ mice [57] (**Supp. Fig 5E-F**). From these results, we conclude that $CD8^+$ T cell dysfunction is not strongly modulated by canonical ColVI receptors.

In the absence of a direct mechanism connecting ColVI receptors to T cell dysfunction, we investigated potential indirect mechanisms. ColVI binds to a number of ECM proteins, including fibrillar collagens such as collagen type I (COLI) [58-62]. COLI, one of the most prevalent collagens in mammalian tissues, is also a potent co-stimulator of effector T cells, strongly inducing $CD8^+$ T cell proliferation when used in conjunction with CD3/T cell receptor stimulation [63]. Therefore, we considered the possibility that Yap1-mediated ColVI deposition promotes $CD8^+$ T cell dysfunction by altering the content and/or organization of ColI in the UPS ECM. We began by examining the architecture of fibrillar collagen molecules in explanted GEMM tumors.

Using multiphoton second harmonic generation (SHG) imaging, we identified significant alterations to fibrillar collagen organization across genotypes, including significantly thinner and straighter fibers in KPY tumors compared to KP (**Fig. 4A-C**). Similar results were observed in SAHA/JQ1-treated compared to control tumors (**Supp. Fig. 6A, B**). We also evaluated human UPS in addition to our GEMMs and found that fibrillar collagen structure in KP tumors recapitulates that of human tumors, confirming that our murine models can successfully reproduce this aspect of tumor biology (**Fig. 4D**, **Mov. S1-3**). Interestingly, however, IHC revealed that ColI content did not significantly differ between KP and KPY tumors, nor between DMSO- and SAHA/JQ1-treated tumors, although a modest (~20%) decrease was observed in KPY (**Fig. 4E, E**, **Supp. Fig 6C-E**). We conclude that sarcoma cell-intrinsic Yap1 impacts the structure/organization of fibrillar collagen networks in the UPS TME, but not ColI quantity.

ColI opposes ColVI and abrogates CD8$^+$ T cell dysfunction

We then specifically examined the relationships among COLI, COLVI, and effector T cell function in greater detail, beginning with UPS patient data from the TCGA dataset. First, although expression of *COL1A1* itself did not track with patient outcomes, expression of *LAIR1*, a co-inhibitory receptor expressed on leukocytes that binds to multiple collagens, including ColI [64], was significantly associated with improved overall survival (**Fig. 4F**, **Supp. Fig. 6F**). Moreover, *LAIR1* gene expression was negatively associated with that of *YAP1* and *COL6A3*, but positively correlated with that of the T cell activation markers *GZMB* and *PRF1* (**Supp. Fig. 6G-J**). Taken together, these correlative clinical data are consistent with our hypothesis that COLVI indirectly suppresses CD8$^+$ T cell function by modulating COLI. To test this hypothesis mechanistically, we developed a novel *in vitro* system by incorporating COLVI into COLI hydrogels (**Fig. 4K**). Activated human CD8$^+$ T cells were cultured on gels containing only COLI, or COLI together with COLVI. Flow cytometry analysis revealed a significant decrease in the percentage of T cells expressing the inhibitory markers PD-1 and TIM-3 (**Fig. 4L, M**) in the presence of COLI alone. COLI-mediated TIM-3 downregulation was also observed as reductions in TIM-3 mean fluorescence intensity (**Supp. Fig. 6G**). Moreover, the proliferative capacity of T cells was improved in the presence of COLI alone, indicated by greater KI67 positivity (**Fig. 4N, O**). Together, these observations indicate that COLI can abrogate the CD8$^+$ T cell dysfunction mediated by COLVI.

Mechanistically, our findings suggest that ColVI functions to restrain ColI-mediated CD8$^+$ T cell activity and proliferation. To test this hypothesis *in vivo*, we generated subcutaneous syngeneic KP tumors expressing control, *Col1a1*- or *Col6a1*-targeting shRNAs in C57BL/6 mice (**Fig. 5A-C**). In this immunocompetent setting, *Col1a1*-deficient tumors grew more rapidly than both control and *Col6a1*-deficient tumors. shCol1a1-tumor-bearing mice also experienced significantly worse survival than mice bearing control tumors, whereas survival of shCol6a1-tumor bearing mice was improved. Similar results were obtained in an immunocompetent orthotopic tumor model (**Fig. 5D**). Impressively, when we assessed the impact of *Col1a1* depletion on KP cell growth *in vitro*, *Col1a1*-deficient cells proliferated more slowly than control cells (**Supp. Fig. 6H**). Thus, these results confirm that the presence of ColI in the UPS ECM controls tumor growth by enabling host anti-tumor immunity, whereas the aberrant deposition of ColVI opposes ColI and promotes immune evasion.

ColVI promotes T cell dysfunction by disrupting CD8$^+$ T cell autophagic flux

To date, an immunosuppressive role of ColVI has not been documented in tumors. We therefore aimed to identify the specific downstream mechanism by which ColVI deposition causes T cell dysfunction. Collagen VI most notably regulates adhesion and migration of a variety of mesenchymal cells [60,65]; however, we were intrigued by the ability of ColVI to modulate autophagy in fibroblasts and muscle tissue [66]. Autophagy is a central regulator of T cell metabolism and is essential for T cell activation [67,68]. To assess whether the presence of ColVI impacted autophagic flux in T cells, we encapsulated T cells in purified COLVI-containing hydrogels and visualized autophagosomes *in situ*. In the presence of COLVI, T cells contained significantly more and brighter autophagosomes than T cells encapsulated in ColI gels (**Fig. 5E-F**). To determine whether COLVI caused autophagosome accumulation by inducing autophagy, or by disrupting autophagic flux and autophagosome clearance, we treated T cells with chloroquine in the presence or absence of COLVI and evaluated LC3B-II expression. In both murine and human T cells, inhibiting autophagic flux with chloroquine did not further increase LC3B-II, indicating that COLVI disrupts autophagic flux, but does not induce autophagy (**Fig 5G**). We confirmed this result by staining for p62, a protein that is rapidly degraded during autophagy induction [69]. Indeed, in the presence of COLVI, p62 accumulated within T cells as evidenced by increased mean p62 signal intensity (**Fig. 5H-I**). Together, these results indicate that extracellular COLVI disrupts autophagic flux in T cells.

COLVI as a potential prognostic and diagnostic biomarker in human STS

To evaluate our experimental findings in the clinical setting, we used data from multiple independent human UPS patient cohorts. Like *YAP1* [39], *COL6A1* is substantially overexpressed in human UPS relative to normal muscle tissue and strongly correlates with poor outcome in UPS patients (**Fig. 6A-C**, **Supp. Fig. 7A**). Similar results were observed for *COL6A2* and *COL6A3* gene expression and patient survival (**Fig. 6D, E**, **Supp. Fig. 7B-G**). We also interrogated the relationship between YAP1 and COLVI in these datasets. Consistent with our *in vitro* and GEMM data demonstrating that Yap1 promotes ColVI deposition in the UPS TME, IHC analysis of surgically resected UPS specimens from the Hospital of the University of Pennsylvania (HUP) revealed that COLVI expression highly correlates with nuclear YAP1 staining, a surrogate for YAP1 transcriptional activity (**Fig. 6F, G**). Similarly, the *COL6A1*, *COL6A2*, and *COL6A3* promoters appear transcriptionally active in these specimens based upon the presence of H3K27Ac marks at these loci (**Fig. 6H**). Moreover, in TCGA specimens, *COL6A3* gene expression positively tracks with that of *YAP1* and *FOXM1* (**Fig. 6I, J**), the latter of which is a *YAP1* target gene in sarcoma.

In this study, we were unable to assess the mechanistic contribution of Yap1-mediated NF-κB signaling to ColVI deposition and T cell function due to the limitations of our *in vivo* models (lack of tumor formation with KPR mice and the potential for confounding Yap1-independent effects with the KPYI "rescue" model). Nevertheless, we have previously shown that the Yap1-NF-κB axis is an essential mediator of sarcomagenesis and progression in human UPS [39,40]. Therefore, we conducted an exploratory analysis of this relationship by examining associations between COLVI deposition and the NF-κB pathway in our human UPS datasets. Through automated IHC analysis, we observed that COLVI protein expression was strongly correlated with nuclear active NF-κB p65 (p65 phospho-S536) staining **(Supp. Fig. 7H, I**). Similarly, *PHLDA1*, an NF-κB target gene in sarcoma, was significantly associated with *COL6A1* and *COL6A3* gene expression **(Supp. Fig. 7J, K**). Moreover, GSEA analysis revealed that the Hallmark "TNFA signaling via NF-κB" gene set was significantly enriched in tumors with above-median *COL6A1*, *COL6A2*, or *COL6A3* gene expression compared to those with below-median expression (**Supp. Fig. 7L**). Thus, relationships between NF-κB and COLVI in UPS phenocopy those between YAP1 and COLVI, illustrating the potential role of YAP1-mediated NF-κB signaling in aberrant ECM remodeling in this tumor subtype.

Finally, we explored the relationship between COLVI expression in UPS and other sarcoma subtypes using a sarcoma tissue microarray (TMA). The mean COLVI H-score of UPS tumors on this TMA (88.52; range: 105.73) was higher than that of all other sarcoma subtypes, and significantly greater than that of leiomyosarcomas, neurofibromas, and synovial sarcomas (**Fig. 7A, B**). Importantly, the dynamic range of COLVI staining in the TMA cohort was similar to that observed in the HUP cohort (H-score range: 142.94). Given that UPS exhibits higher prevalence among adults greater than 50 years of age, and presents with aggressive clinical features such as high tumor grade [33], associations between COLVI H-score and histology were adjusted for patient age, tumor grade, and tumor stage. After controlling for these variables, the aforementioned relationships between COLVI H-score and histologic subtype were attenuated, but remained statistically significant. Tumor grade was the only other variable that exhibited significant associations with COLVI H-score in univariate models. Furthermore, in TCGA dataset, *COL6A1* gene expression was significantly associated with reduced long-term survival among patients with liposarcoma, where COLVI expression levels are similar to those in UPS, but not leiomyosarcoma, where COLVI levels are significantly lower (**Fig. 7C, D**). These data indicate that COLVI expression levels may be a biomarker of long-term clinical outcomes, and sensitivity to immunotherapy, in some human sarcoma patients.

DISCUSSION

Until now, our understanding of the role of the ECM in anti-tumor immunity was primarily limited to ECM-mediated T cell and macrophage migration. Additionally, upstream mediators of aberrant ECM protein composition in the TME were poorly defined. Herein, we establish a more specific understanding of individual collagen molecules in the ECM and adaptive immune cell function in solid tumors (**Fig. 7E**). We discovered that the highly expressed transcriptional co-regulator, YAP1, promotes the deposition of a pro-tumor matrix protein, COLVI, in the UPS ECM. In turn, COLVI alters the organization of anti-neoplastic fibrillar collagen molecules in the TME, namely COLI, thereby disrupting $CD8^+$ T cell autophagic flux and facilitating effector cell dysfunction. Ultimately, our data reveal a novel, non-canonical role of YAP1 in the TME and establish a direct mechanistic link between specific ECM constituents and modulation of immune cell function.

Despite the incredible diversity of the collagen superfamily and the abundance of collagen molecules in solid tumors [27], the effects of specific collagens and other matrix proteins on T cell effector function,

differentiation, and anti-tumor efficacy are poorly characterized. Using murine lung cancer models, Peng et al. [70] demonstrated that extracellular collagen induced $CD8^+$ T cell exhaustion and attenuated responses to α-Pd-1 checkpoint therapy. Although these phenotypes were reversible following inhibition of the collagen cross-linking enzyme LOXL2, the authors did not attribute them to a specific collagen type, in part because LOXL2 inhibition disrupts the synthesis and deposition of multiple collagen species. Additionally, Robertson and colleagues [71] recently showed that incubation of splenocytes with mammary carcinoma cells on collagen type IV (COLIV)-containing matrices may reduce T cell-mediated cancer cell clearance. However, this study [71] did not establish a direct mechanistic link between COLIV and suppression of T cell function, instead suggesting that COLIV may induce a more immunosuppressive transcriptional/secretory profile in mammary carcinoma cells. Moreover, use of mammary carcinoma cells and unstimulated splenocytes from mice of different genetic backgrounds, as well as reliance on transcriptional profiles from mixed carcinoma cell-T cell co-cultures as readouts of T cell function, may have confounded the authors' observations [71]. Conversely, in the present study, we uncovered specific immunomodulatory roles of two distinct collagen species in UPS, and directly linked aberrant ECM composition/organization to induction of $CD8^+$ T cell dysfunction. Remarkably, we discovered that COLVI and COLI possess opposing roles in this tumor context, promoting and opposing immune evasion, respectively. Whereas a direct immunosuppressive role for COLVI has not been previously documented, the COLVI-mediated dysfunction program observed herein upregulated multiple T cell inhibitory receptors (PD1, Tim3, Lag3, CD39) and exhaustion markers (Tcf-1, Tox), suppressed T cell proliferation, and blunted T cell-mediated cytolytic capacity. In contrast, COLI was a tumor suppressor *in vivo*, and reduced $CD8^+$ T cell dysfunction relative to COLVI *in vitro*. These observations are consistent with a prior report in which COLI co-stimulation enhanced effector T cell expansion in a β_1 integrin-dependent manner [63]. Taken together, these results strongly imply that stromal depletion strategies that reduce COLI synthesis/deposition, or that block binding of β integrins on cell surfaces to COLI in the ECM, could elicit detrimental clinical outcomes in human UPS patients.

Given the tumor-suppressive effects of COLI in our study, we were surprised to observe that *LAIR1* gene expression was positively associated with UPS patient survival. Expressed by the majority of peripheral blood mononuclear cells, LAIR1 is a known receptor for numerous collagen species, including COLI [64,72,73]. Binding of LAIR1 to collagens transmits a potent inhibitory signal to leukocytes and can directly inhibit immune

cell activation [73,74]. Notably, however, prior studies of LAIR1-collagen binding have been conducted primarily *in vitro* on collagen-coated dishes and in the presence of leukocyte activating stimuli, enabling co-crosslinking of both activating and inhibitory cell surface receptors [73]. In one *in vivo* study of lung cancer models, binding of collagen in the TME to T cell-expressed integrin b2 upregulated LAIR1 on $CD8^+$ T cells and promoted $CD8^+$ T cell exhaustion [70]. However, a functional role for LAIR1-collagen interactions in mediating exhaustion was not demonstrated [70]. Thus, the survival advantage conferred by high *LAIR1* gene expression in the present study may reflect selective *LAIR1*-mediated inhibition of immunosuppressive cell populations, or an alternative *in vivo* functional role of this receptor. Studies to evaluate the function and collagen-binding mechanisms of LAIR1 *in vivo*, both in the context of tumor antigens and together with soluble and extracellular collagen species, should be performed to address this point.

Senescence, functional exhaustion, insufficient homeostatic proliferation, deletion, and altered metabolism have all been proposed as largely T cell-intrinsic mechanisms that hamper endogenous and engineered T cell-mediated anti-tumor immunity [75]. Our findings offer a novel alternative model in which cancer cell-intrinsic biology drives failure of cytotoxic T cell activity by interfering with T cell autophagic flux. Previous studies have shown that autophagy is rapidly induced upon T cell activation, and that the essential autophagy genes *Atg5* and *Atg7* are critical for the survival, activation, and expansion of mature T cells [76-78]. Moreover, disrupting T cell autophagic flux hinders clearance of damaged mitochondria, resulting in increased reactive oxygen species (ROS) generation and T cell apoptosis [76,78]. Thus, whether and how aberrant ColVI deposition influences ROS production in T cells with dysregulated autophagy is an important direction for future research.

Our study has multiple implications for the clinical management of UPS in human patients. First, as UPS is diagnosed via a process of exclusion, some pleomorphic neoplasms are incorrectly classified as “UPS” when they are more likely to represent pseudosarcomas or high-grade sarcomas with other differentiation lineages [79]. Thus, our observation that COLVI immunostaining is significantly increased in UPS relative to many other soft-tissue sarcoma subtypes indicates that it may be a useful diagnostic tool for distinguishing UPS from other dedifferentiated pleomorphic tumors. Second, our study revealed that PD-1 blockade extended survival of KPY, but not KP mice indicating that anti-PD-1 treatment was not sufficient to reinvigorate dysfunctional effector T cells in KP mice, but did preserve $CD8^+$ T cells with robust cytolytic function in the context of Yap1 deficiency. Together, our findings show that Yap1-mediated signaling can contribute to

immune evasion by modulating the composition and organization of the TME, and indicate that individual collagen species may have unique or opposing effects on UPS patient responses to T cell-based therapies. Specifically, COLVI in the UPS ECM may be detrimental to the efficacy of anti-PD-1 therapy, whereas COLI may potentiate responses to immune checkpoint inhibition. As a result, this study underscores the critical need to systematically evaluate the roles of individual ECM components in the regulation of immune cell function. Furthermore, our data specifically implicate YAP1 and/or COLVI targeting as promising strategies by which to improve the efficacy of checkpoint blockade and other T cell-based therapies in UPS, and potentially other desmoplastic solid tumors.

METHODS

GEMM Tumor models.

All experiments were performed in accordance with NIH guidelines and were approved by the University of Pennsylvania Institutional Animal Care and Use Committee. We generated LSL-*Kras*$^{G12D+}$; *Trp53*$^{fl/fl}$; *YAP1*$^{fl/fl}$ (KPY) and LSL-*Kras*$^{G12D+}$; *Trp53*$^{fl/fl}$; *Rela*$^{fl/fl}$ (KPR) mice by crossing LSL-*Kras*$^{G12D+}$; *Trp53*$^{fl/fl}$ (KP) with *YAP1*$^{fl/fl}$ and *Rela*$^{fl/fl}$ animals. We also created LSL-*Kras*$^{G12D+}$; *Trp53*$^{fl/fl}$; *YAP1*$^{fl/fl}$;LSL-*Ikk2*$^{CA/CA}$ (KPYI) by crossing LSL-*Ikk2*$^{CA/CA}$ (gifted by Foteini Mourkioti, Ph.D.) to KPY. We generated tumors by injection of a calcium phosphate precipitate of adenovirus expressing Cre recombinase (University of Iowa) into the right gastrocnemius muscle of 3-month-old mice.

Microarray and gene set enrichment analysis.

Microarray services were provided by the UPenn Molecular Profiling Facility, including quality control tests of the total RNA samples by Agilent Bioanalyzer and Nanodrop spectrophotometry. All protocols were conducted as described in the Affymetrix WT Plus Reagent Kit Manual and the Affymetrix GeneChip Expression Analysis Technical Manual. Briefly, 250ng of total RNA was converted to first-strand cDNA using reverse transcriptase primed by poly(T) and random oligomers that incorporated the T7 promoter sequence. Second-strand cDNA synthesis was followed by in vitro transcription with T7 RNA polymerase for linear amplification of each transcript, and the resulting cRNA was converted to cDNA, fragmented, assessed by Bioanalyzer, and biotinylated by terminal transferase end labeling. Five and a half micrograms of labeled cDNA were added to Affymetrix hybridization cocktails, heated at 99ºC for 5 min and hybridized for 16 h at 45ºC to Mouse

Transcriptome 1.0 ST GeneChips (Affymetrix Inc., Santa Clara CA) using the GeneChip Hybridization oven 645. The microarrays were then washed at low (6X SSPE) and high (100mM MES, 0.1M NaCl) stringency and stained with streptavidin-phycoerythrin. Fluorescence was amplified by adding biotinylated anti-streptavidin and an additional aliquot of streptavidin-phycoerythrin stain. A GeneChip 3000 7G scanner was used to collect fluorescence signal. Affymetrix Command Console and Expression Console were used to quantitate expression levels for targeted genes; default values provided by Affymetrix were applied to all analysis parameters. Affymetrix cel (probe intensity) files were normalized and summarized using RMA-SST to the gene level using Expression Console software (v1.4.1). Inter sample variation was visualized using Principal Components Analysis in Partek Genomics Suite (v6.6, Partek, Inc., St. Louis, MO). Differential gene expression was tested using Significance Analysis of Microarrays (SAM, samr v2.0), yielding fold change, q-value (false discovery rate) and d-score for each gene. We observed a small number of genes meeting our cutoffs for differential expression and so proceeded to GSEA. Log_2-transformed RMA-sst expression values were used as input to GSEA where enrichment was tested against the hallmark gene sets from the Molecular Signatures Database (MSigDB, v5.1, http://software.broadinstitute.org/gsea/msigdb/index.jsp)

Flow cytometry of murine tumor samples.

Subcutaneous allograft model: Tumors were harvested and minced at indicated time points post-implantation for analysis. Single cell suspensions were generated by digestion with 2 mg/mL collagenase B (Roche #11088823103) and 30 U/ml DNAse I for 45 minutes at 37°C and filtration through 70 uM cell strainer. RBCs were lysed using ACK lysis buffer. Samples were incubated for 5 minutes at room temperature with anti-mouse CD16/32 Fc Block, and subsequently stained on ice with primary fluorophore-conjugated antibodies for identification of cell populations by flow cytometry. 7AAD (BioLegend) was used for dead cell discrimination. Flow cytometry was performed on an LSR II Flow Cytometer (BD Biosciences) and analyzed using FlowJo software (BD biosciences).

Orthotopic model: Single-cell suspensions from bulk tumors were generated as described above. RBC lysis was performed as indicated above, after which samples were incubated with anti-mouse CD16/32 Fc block for 10 minutes on ice (1 uL FC block/1 x 10^6 cells). T cell enrichment was then performed using the mouse CD3ε microbead kit with LD columns (Miltenyi Biotech). T cell-enriched cell populations were then eluted from the columns and stained with LIVE/DEAD Fixable Aqua Dead Cell Dye (Thermo Fisher) for dead cell

discrimination. Subsequently, extracellular staining was performed with pre-titrated fluorescent-conjugated antibodies on ice for 30 minutes, followed by fixation and permeabilization (eBioscience Foxp3/Transcription Factor Staining Buffer Set), and intracellular staining (1 hour at room temperature). Data were acquired with a FACSymphony A3 Lite cytometer (BD) and analyzed with FlowJo software. Single-color compensation controls were generated with UltraComp eBeads Plus Compensation beads, and identification of positive and negative populations were determined through the use of fluorescence-minus-one (FMO) controls. Antibody and signal detection information pertaining to this panel are provided in Supplemental Table 2.

Cell lines.

HEK-293T cell lines were purchased from ATCC (Manassas, VA, USA). STS-109 cells were derived from a human UPS tumor by Rebecca Gladdy, M.D. (University of Toronto). KP230 cell lines were derived from UPS mouse tumors as described previously by David Kirsch M.D., Ph.D. (Duke University). STR analysis was performed at the time of derivation and confirmed in April 2015. Cells were purchased, thawed, and then expanded in the laboratory. Multiple aliquots were frozen down within 10 days of initial resuscitation. For experimental use, aliquots were resuscitated and cultured for up to 20 passages (4–6 wk) before being discarded. STS109 cells were cultured in DMEM with 20% (vol/vol) FBS, 1% L-glutamine, and 1% penicillin/streptomycin; other cells were cultured in DMEM with 10% (vol/vol) FBS, 1% L-glutamine, and 1% penicillin/streptomycin. MEFs were cultured as previously reported in [80]. All cell lines were confirmed to be negative for mycoplasma contamination.

Two Photon Second Harmonic Generation Imaging of tumors.

Orientation and distribution of collagen fibers were visualized with second harmonic generation (SHG) using a Leica TCS SP8MP 2-photon microscope (Leica Microsystems, Buffalo Grove, Il) equipped with a Chameleon femtosecond-pulsed laser (Coherent, Inc, Santa Clara, CA.). 960nm excitation was used to create better signal separation from endogenous autofluorescence. SHG signal was collected with a HyD detector through a DAPI filter cube, while autofluorescent signals were collected through FITC and TRITC filter cubes with standard PMTs and used to determine background separation. Freshly excised tumors, maintained in phosphate buffered saline, were cut in half and imaged to a depth of 100um in random areas across the cut surface using a 25X 1.0NA water immersion objective. Selected 5um stacks with even illumination, derived from the original, were used for quantification. Alternatively, tumor tissues were fixed for 48hrs in 4% neutral buffered

paraformaldehyde, embedded in paraffin, sectioned at 7-10um, collected on glass slides and allowed to set. The unstained and unmounted tissues were then imaged as described above. 5-7um stacks were acquired in 1um steps at each location and 5um subset stacks were further processed for analysis. Each image stack was deconvolved with Huygens software (Scientific Volume Imaging, Hilversum, The Netherlands) and quantified with Leica LASX software using a standardized macro algorithm to determine total area of collagen within each measured area.

Collagen fiber analysis.

Collagen fiber width and linearity were analyzed using a ct-Fire analysis, a previously established method on SHG images of tumors reported in [81]. The software segments the image and calculates intensity gradients within subregions of images and uses them to track the overall directions of fibers. Linearity of fibers was calculated by overall displacement between the start and end of the fiber divided by the total length of the fiber.

Drug Treatments and Reagents.

Cells were treated with SAHA (2μM) (Sigma Aldrich) and JQ1 (0.5μM) (gift from Jun Qi, Ph.D., Harvard University) in combination for the time indicated in the figure legends. Drugs were refreshed for any cells treated for longer than 48hrs.

Lentiviral Transduction.

Glycerol stocks for shRNA-mediated knockdown of *Yap1* TRCN: 0000095864, 0000095866, 0000095867, 0000095868; *YAP1* TRCN: 0000107266, 0000107267; *Rela* (p65 NF-κB) TRCN:0000055343, 0000055344, 0000055347; *Col6a1* TRCN: 0000091533, 0000091535, 0000091536; *COL6A1* TRCN: 0000116957, 0000116961; *Col1a1* TRCN: TRCN0000090505, TRCN0000090507; and scramble shRNA were obtained from Sigma Aldrich. shRNA plasmids were packaged using the third-generation lenti-vector system (pMDLg/pRRE, pRSV-Rev, and pMD2.G/VSVG) and expressed in HEK-293T cells. Supernatant was collected at 24 and 48 hrs. after transfection and subsequently concentrated using 10-kDa Amicon Ultra-15 centrifugal filter units (Millipore) or polyethylene glycol-8000. Transduction of target cells was performed in the presence of 7.5–8.0 μg/mL polybrene (Sigma-Aldrich, #H9268).

Immunohistochemistry.

Paraffin embedded tissues were stained using 5 micron tissue sections and the BOND-MAX Leica automated IHC/ISH stainer. Stained slides were digitally scanned by the Pathology Core Laboratory at the Children's

Hospital of Philadelphia or the University of Pennsylvania School of Veterinary Medicine Comparative Pathology Core. Aperio ImageScope (Leica Biosystems, USA) software was used for slide quantification. For CD4, CD8, Foxp3, and B220, the nuclear v9 algorithm was used to quantify cell positivity. The positive pixel count algorithm was used to quantify F4/80, ColVI and Col1a1 staining in murine tissue. Digital analysis of YAP1, COLVI, and p-p65 staining in human tissue is described in detail in the Immunohistochemistry Appendix that accompanies this manuscript. The following antibodies and dilutions were used: rat anti-Foxp3 (eBioscience #17-5773-82; 1:100), rat anti-F4/80 (Invitrogen #MF48000; 1:25), rabbit anti-CD4 (Cell Signaling #25229; 1:100), rabbit anti-CD8 (Cell Signaling #98941; 1:100), rat anti-B220 (BD Pharmingen #557390; 1:100), rabbit anti-Collagen VI (Abcam #6588; 1:100 [mouse and human tissue]), rabbit anti-YAP1 (Cell Signaling #14074; 1:100), rabbit anti-NF-κB p65 phospho-S536 (Abcam #86299; 1:100), and anti-COL1 (Boster Bio PA2140-2, 5 ug/mL).

Immunoblots.

Protein lysate was prepared in SDS/Tris (pH7.6) lysis buffer, separated by electrophoresis in 8-10% SDS/PAGE gels, transferred to nitrocellulose membrane, and probed with the following antibodies: rabbit anti-YAP1 (Cell signaling #4912; 1:1,000), rabbit anti-COL6A1 (Proteintech #17023-1-AP; 1:1,000), rabbit anti-COL6A2 (NOVUS #NBP1-90951; 1:500), rabbit anti-GAPDH (Cell signaling #2118; 1:10,000), and rabbit anti-LC3B (R&D MAB85582 1:5000).

Oncomine, TCGA survival and cBioPortal analysis.

We used the publicly available dataset published in Detwiller et al. through Oncomine Research Premium edition software (version 4.5, Life Technologies) to query ColVI gene expression in sarcoma and normal muscle tissue. Kaplan-Meier survival analyses using TCGA data were conducted using gene expression values ranked according to the rlog transformation. Kaplan-Meier analyses were performed for overall, disease-free, and disease-specific survival of patients. Gene expression correlations were conducting using TCGA gene expression data normalized with DESeq 2. Clinical data were downloaded from the "Adult Soft Tissue Sarcomas (TCGA, Cell 2017)" [48] cBioPortal dataset on March 21, 2019.

Human samples.

Human sarcoma or non-malignant muscle samples were obtained from surgically resected tumors from patients (de-identified) undergoing therapeutic surgical resection in accordance with protocols approved by the Institutional Review Board at the University of Pennsylvania.

ChIP-seq.

For tumor samples resected from UPS patients at the Hospital of the University of Pennsylvania, approximately 100 mg of tissue was minced into 1-2 mm pieces and incubated in 1% formaldehyde for 15 minutes. Formaldehyde was quenched with glycine at 0.125 M. Fixed tissue was homogenized for 60 seconds with a Tissue Tearor Homogenizer (Biospec) at 30,000 RPM. Homogenized tissue was washed with ice-cold PBS with 1X HALT protease inhibitor. For cell-line ChIP-RX, samples were fixed for 10 minutes in 1% formaldehyde quenched with glycine and washed with PBS as above. 5e6 S2 cells (Drosophila Melanogaster) were added to each sample of 2.5e7 for ChIP-RX normalization in downstream analysis.

Cell proliferation assay.

1 x 10^3 cells per well were plated in a 96-well plate and growth was monitored using the PrestoBlue Cell viability kit (Invitrogen #A13261).

RNA isolation and analysis.

Total RNA was isolated from tissues and cells using the Trizol reagent (Life Technologies) and RNeasy Mini Kit (Qiagen). Revere transcription of mRNA was performed using the High-Capacity RNA-to-cDNA Kit (Life Technologies). qRT-PCR was performed by using a ViiA7 real-time PCR system (Applied Biosystems). All probes were obtained from TaqMan “Best coverage” (Life Technologies). HPRT or SDHA were used as an endogenous control. For bulk tumor qRT-PCR, two 10-mg tissue samples were taken per murine tumor for analysis of each TaqMan probe.

Implantation of tumor cells, tumor growth measurements and survival analyses

Cultured KP cells (pure C57BL/6 background, a gift from Sandra Ryeom, Ph.D., University of Pennsylvania) were detached using 0.05% trypsin (GIBCO), washed once with DMEM media and once with 1x PBS, and counted in preparation for implantation. 0.5×10^6 tumor cells were implanted subcutaneously (s.c.) or orthotopically (Intramuscular, IM) into shaved flanks of recipient C57BL/6 mice. Tumor dimensions were measured using calipers starting at day 7 and every three days thereafter; volume was calculated using the

formula $(ab^2)\pi/2$, where a is the longest measurement and b is the shortest. Tumor volumes of $1500mm^3$ were used as endpoints for survival analyses.

Fabrication of Collagen Gels.

Collagen gel was prepared as reported previously in [11] with the following modifications. Rat tail collagen type I (Corning stock concentration 9.41 mg/mL) was mixed with native human collagen type VI (1.0 mg/mL) (Rockland 009-001-108) or an equivalent volume of acetic acid as well as 10x Medium 199 buffer (ThermoFisher #11825015). The solution was neutralized with 1M NaOH dropwise and mixed with 1x M199 buffer (ThermoFisher #11043023). The final concentration of collagen I was 1.5 mg/mL and collagen VI concentrations varied according to experimental conditions. Gels were polymerized at 37 °C for 30 minutes. Gels were then washed with PBS prior to incubation with cells. For blocking assays, activated human $CD8^+$ T cells were incubated with anti-NG2 (clone 9.2.27, Santa Cruz Biotechnology, 40 μg/mL), anti-ITGB1 (clone P5D2, R&D Systems, 10 μg/mL), or the corresponding isotype control (IgG2a and IgG1, respectively) for 1 hour at 37 degrees prior to encapsulation in hydrogels. Alternatively, cells were treated with cilengitide (10 μg/mL, Tocris Bioscience) to block integrin $\alpha v\beta 3$ or vehicle control. Cells were analyzed for expression of dysfunction markers and KI67 24 hours after encapsulation via flow cytometry.

Generation of decellularized ECMs

Glass-bottom chamber slides were coated with 0.2% gelatin for 1h at 37°C, followed by 2.5% glutaraldehyde at room temperature for 30 minutes. The plate was washed twice with PBS and 50,000 cells were seeded. Media was supplemented with 50 ug/mL L-ascorbic acid (Sigma a7506) and changed daily. Cells were maintained for 7 days in hypoxic conditions (1% oxygen). The decellularization protocol is adapted from Harris et. al [82]. Briefly, cells were washed twice with the wash buffer 1 described prior to lysis with NP-40 based lysis buffer. Cell debris were removed with wash buffer 2 prior to four final washes with DI water. ECMs were stored at 4 °C in PBS.

Immunofluorescence.

To quantify collagen VI expression differences in decellularized ECMs, the ECMs were stained with rabbit anti-Collagen VI (Abcam #ab6588; 1:1000) overnight at 4°C and goat anti-rabbit (H+L) secondary antibody, Alexa Fluor 546 (ThermoFisher #A-11035; 1:1000) for 30 minutes at room temperature. For hydrogels, mouse anti-

p62 (R&D MAB8028 1:250) was incubated overnight at 4°C prior to goat anti-mouse (H+L) secondary antibody, Alexa Fluor 488 (ThermoFisher #A-11035; 1:500) for 1 hour at room temperature.

T cell culture.

Human CD8+ T cells were purchased from Astarte bioscience and cultured in RPMI with 10% FBS, IL-2, and penicillin/streptomycin. T cells were activated for 4 days using human T cell stimulator (CD3/CD28) Dynabeads (ThermoFisher 11161D) prior to experiments.

Murine T cell isolation and activation.

$CD8^+$ T cells were isolated from spleens of 6-12 weeks old C57BL/6 mice. C57BL/6J mice were maintained per guidelines approved by the Johns Hopkins University's Institutional Review Board. Cells were macerated through cell filters using a syringe and treated with ACK lysing buffer for erythrocyte lysis and to isolate splenocytes. CD8+ T lymphocytes were isolated from splenocytes by negative selection using CD8+ isolation kits (130-104-075) and magnetic columns from Miltenyi Biotech (Auburn, CA, USA) according to the manufacturer's protocol. Cells were cultured in RPMI containing 10% FBS, penicillin/streptomycin, and IL-2 (40 U/mL). Activated $CD8^+$ cells were incubated with decellularized ECMs immediately after isolation in culture media without IL-2 for 48 hours prior to flow cytometry analysis.

Flow Cytometry of isolated T cells.

Human T cells were stained with CD44 BB515 (clone G44-26 BD bioscience), CD62L APC (clone DREG-56 Biolegend), and CD45RA PE (clone HI100 Biolegend). Gating on positive populations was determined using fluorescence-minus-one controls. Data were acquired on a BD FACS Canto II (BD biosciences). Data was analyzed with FCS express. Murine cells were stained with CD44 FITC (clone IM7 Biolegend), CD62L APC-Cy7 (clone MEL-14 BD Biosciences), TIM-3 PE-Cy7 (clone B8.2C12 Biolegend), PD-1 PE (clone 29F.1A12 Biolegend), CD3 APC (clone 17A2 Biolegend), CD8a PerCP (clone 53-6.7 Biolegend), Ki67 AlexaFluor-488 (clone SolA15 Thermo Fisher). For experiments on decellularized ECMs cells were gated on viable cells (FSC-A versus SSC-A), then single cells (FSC-A versus FSC-H), then T cell markers (CD3 versus CD8). Gating on positive populations was determined using "Fluorescence Minus One" controls. Data was acquired on a BD FACS Canto II or LSRII (BD biosciences). Data was analyzed with FlowJo Software.

Depletion of $CD8^+$ T cells *in vivo*

200ug of clone 2.43 ($CD8^+$ T cell depletion), or clone LTF-2 (isotype control) antibody was administered i.p. starting three days prior to tumor implantation and repeated every three days until mouse sacrifice. All antibodies were purchased from BioXCell. $CD8^+$ depletion was confirmed in peripheral blood.

CART cell preparation.

CART-TnMUC1 T cells [52] and donor-matched untransduced (NTD) cells were thawed in a 37°C water bath. T cells were resuspended in STS-109 culture medium. Cells were subsequently centrifuged for 5 minutes at 500 x g. This was done twice to remove residual cryopreservants. Cell pellets were then resuspended in culture media at a final concentration of 1 x 10^6 cells/mL and rested overnight at 37°C in 5% CO_2.

xCELLigence real-time target cell cytotoxicity analysis.

For the xCELLigence real-time target cell cytotoxicity assay, STS109 targets were harvested and seeded in triplicate into 96-well polyethylene terephthalate plates (E-Plate VIEW 96 PET) at 5,000 total targets per well. Cells were allowed to adhere to the bottoms of wells for 24 hours (37°C, 5% CO_2 conditions). Adhesion of cells to the gold microelectrodes in the E-Plates impedes the flow of electric current between electrodes. This impedance value, plotted as a unitless parameter known as “Cell Index”, increases as cells proliferate and then plateaus as cells approach 100% confluence. Effector cells (CART-TnMUC1cells or NTD T cells) were added to wells containing the appropriate targets at E:T cell ratios of 10:1, 5:1, 1:1, and 0:1. These non-adherent effector cells in suspension do not cause impedance changes in and of themselves (due to lack of adherence to the gold microelectrodes). In these experiments, target cells lysed by 1% Triton-X-100 were used as the positive control, while NTD cells at the same E:T ratios listed above were assayed as negative controls. Cytotoxic activity of the T lymphocytes was determined via continuous acquisition of impedance data for each well containing target cells over 6 days. Raw impedance data was analyzed using RTCA 2.1.0 software. Curves indicate the percent (%) Cytolysis using NTD controls as a reference. The curves also subtract the signal from wells containing effector cells alone and from wells containing target cells treated with a rapid killing agent (i.e., Triton-X-100) to compensate for residual background signal. The general equation for calculating the % Cytolysis for a sample at a time point *t* is: $\% \text{ Cytolysis}_{st} = [1-(NCI_{st})/(AvgNCI_{Rt})]x100$, where, NCI_{st} is the Normalized Cell Index for the sample and NCI_{Rt} is the average of Normalize Cell Index for the matching reference wells.

***In vivo* reagents.**

In checkpoint studies 200ug of anti-PD1 monoclonal blocking antibody (clone RMP 1-14, BioXCell) or isotype control antibody (clone 2A3, BioXCell) was administered i.p. at days 7, 10 and once tumors reached 100 mm^3. In SAHA/JQ1 studies, total 44 (n=11 per group) autochthonous KP mice were randomly divided into 4 groups to receive different treatments once tumors reached 100 mm^3, and injected for up to 20 days. The mice were euthanized 24hrs after the tumor volume reached 2000 mm^3). 1) Vehicle group (10% Hydroxypropyl-β-cyclodextrin plus DMSO was diluted daily in sterile 45% PEG/55% H_2O); 2). JQ1 group (JQ1 was diluted daily in 10% HP-β-CD injected into the peritoneal cavity 25 mg/kg twice daily); 3). SAHA group (SAHA was diluted in sterile 45% PEG/55% H_2O injected into the peritoneal cavity 50 mg/kg daily); 4). JQ1 and SAHA combination treatment group (drugs were diluted in their respective vehicles). Treatment method for drug combination group: 1). 25mg/kg SAHA+50mg/kg JQ1 for the first 5 days. 2) 25mg/kg SAHA+25mg/kg JQ1 each other day for 10 days. 3). 25mg/kg SAHA+50mg/kg JQ1 for 2 days. 4). Then mice with tumors received 25mg/kg SAHA with 25mg/kg JQ1 for 3 days. Mice without tumors received 5mg/kg SAHA and 5mg/kg JQ1 for 3 days). JQ1 was provided by Jun Qi (Dana-Farber Cancer Institute) and SAHA was purchased from Cayman Chemical. HP-β-CD and PEG400 were obtained from Sigma-Aldrich.

Autophagy Detection

The Cyto-ID Autophagy detection kit 2.0 (Enzo Life Sciences) was used to assess autophagic vacuoles according to the manufacturer's instructions with the following modifications. CytoID containing media (1:500) was overlaid onto hydrogels containing activated CD8+ T cells for 30 minutes at 37 degrees Celsius. Media was replaced and cells were incubated for 4 hours prior to fixation with 4% PFA. Cells were then stained with Phalloidin-AlexaFluor 546 (1:500) and DAPI (1:1000) to localize individual cells and imaged on a Zeiss LSM780 confocal at 40x magnification. Vacuole number and intensity was quantified using Imaris 8.3.1.

Statistical Analysis.

Statistical analysis was performed using Prism (Graph Pad Software). Data are shown as mean ± SEM or SD. Data were reported as biological replicates, with technical replicates indicated in figure legends. Student *t*-tests (unpaired two-tailed) were performed to determine whether the difference between two means was statistically significant, with a *P*-value <0.05 considered significant. ANOVA was used for assays with three or more groups. 2-way repeated-measures ANOVA was used for *in vivo* tumor growth curves. For correlations,

Spearman's coefficient was used if at least one dataset was not normally distributed. Pearson's coefficient was used if both datsets were normally distributed. Shapiro-Wilk test was used to assess normality.

REFERENCES

1 Blank, C. U. *et al.* Defining 'T cell exhaustion'. *Nat Rev Immunol* **19**, 665-674, doi:10.1038/s41577-019-0221-9 (2019).

2 Zhao, Y., Shao, Q. & Peng, G. Exhaustion and senescence: two crucial dysfunctional states of T cells in the tumor microenvironment. *Cell Mol Immunol* **17**, 27-35, doi:10.1038/s41423-019-0344-8 (2020).

3 Thommen, D. S. & Schumacher, T. N. T Cell Dysfunction in Cancer. *Cancer Cell* **33**, 547-562, doi:10.1016/j.ccell.2018.03.012 (2018).

4 Katz, D., Palmerini, E. & Pollack, S. M. More Than 50 Subtypes of Soft Tissue Sarcoma: Paving the Path for Histology-Driven Treatments. *Am Soc Clin Oncol Educ Book* **38**, 925-938, doi:10.1200/EDBK_205423 (2018).

5 Fletcher, C. D. M., World Health Organization. & International Agency for Research on Cancer. *WHO classification of tumours of soft tissue and bone*. 4th edn, (IARC Press, 2013).

6 Taylor, B. S. *et al.* Advances in sarcoma genomics and new therapeutic targets. *Nat Rev Cancer* **11**, 541-557, doi:10.1038/nrc3087 (2011).

7 Eisinger-Mathason, T. S. *et al.* Hypoxia-dependent modification of collagen networks promotes sarcoma metastasis. *Cancer Discov* **3**, 1190-1205, doi:10.1158/2159-8290.CD-13-0118 (2013).

8 Pankova, V., Thway, K., Jones, R. L. & Huang, P. H. The Extracellular Matrix in Soft Tissue Sarcomas: Pathobiology and Cellular Signalling. *Front Cell Dev Biol* **9**, 763640, doi:10.3389/fcell.2021.763640 (2021).

9 Baird, K. *et al.* Gene expression profiling of human sarcomas: insights into sarcoma biology. *Cancer Res* **65**, 9226-9235, doi:10.1158/0008-5472.CAN-05-1699 (2005).

10 Pepin, K. *et al.* Soft Tissue Sarcoma Stiffness and Perfusion Evaluation by MRE and DCE-MRI for Radiation Therapy Response Assessment: A Technical Feasibility Study. *Biomed Phys Eng Express* **5**, doi:10.1088/2057-1976/ab2175 (2019).

11 Lewis, D. M. *et al.* A Feedback Loop between Hypoxia and Matrix Stress Relaxation Increases Oxygen-Axis Migration and Metastasis in Sarcoma. *Cancer Res* **79**, 1981-1995, doi:10.1158/0008-5472.CAN-18-1984 (2019).

12 Owusu-Ansah, K. G. *et al.* COL6A1 promotes metastasis and predicts poor prognosis in patients with pancreatic cancer. *Int J Oncol* **55**, 391-404, doi:10.3892/ijo.2019.4825 (2019).

13 Turtoi, A. *et al.* Accessibilome of human glioblastoma: collagen-VI-alpha-1 is a new target and a marker of poor outcome. *J Proteome Res* **13**, 5660-5669, doi:10.1021/pr500657w (2014).

14 Wan, F. *et al.* Upregulation of COL6A1 is predictive of poor prognosis in clear cell renal cell carcinoma patients. *Oncotarget* **6**, 27378-27387, doi:10.18632/oncotarget.4860 (2015).

15 Zhu, Y. P. *et al.* Reactive stroma component COL6A1 is upregulated in castration-resistant prostate cancer and promotes tumor growth. *Oncotarget* **6**, 14488-14496, doi:10.18632/oncotarget.3697 (2015).

16 Mak, P. *et al.* ERbeta impedes prostate cancer EMT by destabilizing HIF-1alpha and inhibiting VEGF-mediated snail nuclear localization: implications for Gleason grading. *Cancer Cell* **17**, 319-332, doi:S1535-6108(10)00082-6 [pii]
10.1016/j.ccr.2010.02.030 (2010).

17 Rhim, A. D. *et al.* EMT and dissemination precede pancreatic tumor formation. *Cell* **148**, 349-361, doi:10.1016/j.cell.2011.11.025
S0092-8674(11)01369-9 [pii] (2012).

18 Schrader, J. *et al.* Matrix stiffness modulates proliferation, chemotherapeutic response, and dormancy in hepatocellular carcinoma cells. *Hepatology* **53**, 1192-1205, doi:10.1002/hep.24108 (2011).

19 Seguin, L. *et al.* An integrin beta(3)-KRAS-RalB complex drives tumour stemness and resistance to EGFR inhibition. *Nat Cell Biol* **16**, 457-468, doi:10.1038/ncb2953 (2014).

20 Lesniak, D. *et al.* Beta1-integrin circumvents the antiproliferative effects of trastuzumab in human epidermal growth factor receptor-2-positive breast cancer. *Cancer Res* **69**, 8620-8628, doi:10.1158/0008-5472.CAN-09-1591 (2009).

21 Kanda, R. *et al.* Erlotinib resistance in lung cancer cells mediated by integrin beta1/Src/Akt-driven bypass signaling. *Cancer Res* **73**, 6243-6253, doi:10.1158/0008-5472.CAN-12-4502 (2013).
22 Huang, C. *et al.* beta1 integrin mediates an alternative survival pathway in breast cancer cells resistant to lapatinib. *Breast Cancer Res* **13**, R84, doi:10.1186/bcr2936 (2011).
23 Jensen, C. *et al.* Non-invasive biomarkers derived from the extracellular matrix associate with response to immune checkpoint blockade (anti-CTLA-4) in metastatic melanoma patients. *J Immunother Cancer* **6**, 152, doi:10.1186/s40425-018-0474-z (2018).
24 Pruitt, H. C. *et al.* Collagen fiber structure guides 3D motility of cytotoxic T lymphocytes. *Matrix Biol*, doi:10.1016/j.matbio.2019.02.003 (2019).
25 Thomas, A. H., Edelman, E. R. & Stultz, C. M. Collagen fragments modulate innate immunity. *Exp Biol Med (Maywood)* **232**, 406-411 (2007).
26 Nicolas-Boluda, A. *et al.* Tumor stiffening reversion through collagen crosslinking inhibition improves T cell migration and anti-PD-1 treatment. *Elife* **10**, doi:10.7554/eLife.58688 (2021).
27 Ricard-Blum, S. The collagen family. *Cold Spring Harb Perspect Biol* **3**, a004978, doi:10.1101/cshperspect.a004978 (2011).
28 Armstrong, T. *et al.* Type I collagen promotes the malignant phenotype of pancreatic ductal adenocarcinoma. *Clin Cancer Res* **10**, 7427-7437, doi:10.1158/1078-0432.CCR-03-0825 (2004).
29 Olive, K. P. *et al.* Inhibition of Hedgehog signaling enhances delivery of chemotherapy in a mouse model of pancreatic cancer. *Science* **324**, 1457-1461, doi:10.1126/science.1171362 (2009).
30 Honma, K., Miyata, T. & Ochiya, T. Type I collagen gene suppresses tumor growth and invasion of malignant human glioma cells. *Cancer Cell Int* **7**, 12, doi:10.1186/1475-2867-7-12 (2007).
31 Ozdemir, B. C. *et al.* Depletion of carcinoma-associated fibroblasts and fibrosis induces immunosuppression and accelerates pancreas cancer with reduced survival. *Cancer Cell* **25**, 719-734, doi:10.1016/j.ccr.2014.04.005 (2014).
32 Bhattacharjee, S. *et al.* Tumor restriction by type I collagen opposes tumor-promoting effects of cancer-associated fibroblasts. *J Clin Invest* **131**, doi:10.1172/JCI146987 (2021).
33 Widemann, B. C. & Italiano, A. Biology and Management of Undifferentiated Pleomorphic Sarcoma, Myxofibrosarcoma, and Malignant Peripheral Nerve Sheath Tumors: State of the Art and Perspectives. *J Clin Oncol* **36**, 160-167, doi:10.1200/JCO.2017.75.3467 (2018).
34 Tawbi, H. A. *et al.* Pembrolizumab in advanced soft-tissue sarcoma and bone sarcoma (SARC028): a multicentre, two-cohort, single-arm, open-label, phase 2 trial. *Lancet Oncol* **18**, 1493-1501, doi:10.1016/S1470-2045(17)30624-1 (2017).
35 Arora, S., Rastogi, S., Shamim, S. A., Barwad, A. & Sethi, M. Good and sustained response to pembrolizumab and pazopanib in advanced undifferentiated pleomorphic sarcoma: a case report. *Clin Sarcoma Res* **10**, 10, doi:10.1186/s13569-020-00133-9 (2020).
36 Cheung, L. S. *et al.* Anti-PD-1 elicits regression of undifferentiated pleomorphic sarcomas with UV-mutation signatures. *J Immunother Cancer* **9**, doi:10.1136/jitc-2021-002345 (2021).
37 Keung, E. Z. *et al.* Phase II study of neoadjuvant checkpoint blockade in patients with surgically resectable undifferentiated pleomorphic sarcoma and dedifferentiated liposarcoma. *BMC Cancer* **18**, 913, doi:10.1186/s12885-018-4829-0 (2018).
38 Ye, S. *et al.* TGFbeta and Hippo Pathways Cooperate to Enhance Sarcomagenesis and Metastasis through the Hyaluronan-Mediated Motility Receptor (HMMR). *Mol Cancer Res*, doi:10.1158/1541-7786.MCR-19-0877 (2020).
39 Ye, S. *et al.* YAP1-mediated suppression of USP31 enhances NF-kappaB activity to promote sarcomagenesis. *Cancer Res*, doi:10.1158/0008-5472.CAN-17-4052 (2018).
40 Rivera-Reyes, A. *et al.* YAP1 enhances NF-kappaB-dependent and independent effects on clock-mediated unfolded protein responses and autophagy in sarcoma. *Cell Death Dis* **9**, 1108, doi:10.1038/s41419-018-1142-4 (2018).
41 Eisinger-Mathason, T. S. *et al.* Deregulation of the Hippo pathway in soft-tissue sarcoma promotes FOXM1 expression and tumorigenesis. *Proc Natl Acad Sci U S A* **112**, E3402-3411, doi:10.1073/pnas.1420005112 (2015).
42 Murakami, S. *et al.* Yes-associated protein mediates immune reprogramming in pancreatic ductal adenocarcinoma. *Oncogene* **36**, 1232-1244, doi:10.1038/onc.2016.288 (2017).
43 Kim, W. *et al.* Hepatic Hippo signaling inhibits protumoural microenvironment to suppress hepatocellular carcinoma. *Gut* **67**, 1692-1703, doi:10.1136/gutjnl-2017-314061 (2018).

44 Zhou, T. Y. *et al.* Interleukin-6 induced by YAP in hepatocellular carcinoma cells recruits tumor-associated macrophages. *J Pharmacol Sci* **138**, 89-95, doi:10.1016/j.jphs.2018.07.013 (2018).
45 Elosegui-Artola, A. *et al.* Force Triggers YAP Nuclear Entry by Regulating Transport across Nuclear Pores. *Cell* **171**, 1397-1410 e1314, doi:10.1016/j.cell.2017.10.008 (2017).
46 Kirsch, D. G. *et al.* A spatially and temporally restricted mouse model of soft tissue sarcoma. *Nat Med* **13**, 992-997, doi:10.1038/nm1602 (2007).
47 Mito, J. K. *et al.* Cross species genomic analysis identifies a mouse model as undifferentiated pleomorphic sarcoma/malignant fibrous histiocytoma. *PLoS One* **4**, e8075, doi:10.1371/journal.pone.0008075 (2009).
48 Cancer Genome Atlas Research Network. Electronic address, e. d. s. c. & Cancer Genome Atlas Research, N. Comprehensive and Integrated Genomic Characterization of Adult Soft Tissue Sarcomas. *Cell* **171**, 950-965 e928, doi:10.1016/j.cell.2017.10.014 (2017).
49 Serrano, C. *et al.* RAS/MAPK pathway hyperactivation determines poor prognosis in undifferentiated pleomorphic sarcomas. *Cancer* **122**, 99-107, doi:10.1002/cncr.29733 (2016).
50 Hoesel, B. & Schmid, J. A. The complexity of NF-kappaB signaling in inflammation and cancer. *Mol Cancer* **12**, 86, doi:10.1186/1476-4598-12-86 (2013).
51 Jiang, Y., Li, Y. & Zhu, B. T-cell exhaustion in the tumor microenvironment. *Cell Death Dis* **6**, e1792, doi:10.1038/cddis.2015.162 (2015).
52 Posey, A. D., Jr. *et al.* Engineered CAR T Cells Targeting the Cancer-Associated Tn-Glycoform of the Membrane Mucin MUC1 Control Adenocarcinoma. *Immunity* **44**, 1444-1454, doi:10.1016/j.immuni.2016.05.014 (2016).
53 Low, B. C. *et al.* YAP/TAZ as mechanosensors and mechanotransducers in regulating organ size and tumor growth. *FEBS Lett* **588**, 2663-2670, doi:10.1016/j.febslet.2014.04.012 (2014).
54 Bonaldo, P. *et al.* Collagen VI deficiency induces early onset myopathy in the mouse: an animal model for Bethlem myopathy. *Hum Mol Genet* **7**, 2135-2140, doi:10.1093/hmg/7.13.2135 (1998).
55 Schnoor, M. *et al.* Production of type VI collagen by human macrophages: a new dimension in macrophage functional heterogeneity. *J Immunol* **180**, 5707-5719, doi:10.4049/jimmunol.180.8.5707 (2008).
56 Mas-Moruno, C., Rechenmacher, F. & Kessler, H. Cilengitide: the first anti-angiogenic small molecule drug candidate design, synthesis and clinical evaluation. *Anticancer Agents Med Chem* **10**, 753-768, doi:10.2174/187152010794728639 (2010).
57 Liu, S. *et al.* Capillary morphogenesis protein-2 is the major receptor mediating lethality of anthrax toxin in vivo. *Proc Natl Acad Sci U S A* **106**, 12424-12429, doi:10.1073/pnas.0905409106 (2009).
58 Keene, D. R., Ridgway, C. C. & Iozzo, R. V. Type VI microfilaments interact with a specific region of banded collagen fibrils in skin. *J Histochem Cytochem* **46**, 215-220, doi:10.1177/002215549804600210 (1998).
59 Kuo, H. J., Maslen, C. L., Keene, D. R. & Glanville, R. W. Type VI collagen anchors endothelial basement membranes by interacting with type IV collagen. *J Biol Chem* **272**, 26522-26529, doi:10.1074/jbc.272.42.26522 (1997).
60 Sardone, F. *et al.* Collagen VI-NG2 axis in human tendon fibroblasts under conditions mimicking injury response. *Matrix Biol* **55**, 90-105, doi:10.1016/j.matbio.2016.02.012 (2016).
61 Lettmann, S. *et al.* Col6a1 null mice as a model to study skin phenotypes in patients with collagen VI related myopathies: expression of classical and novel collagen VI variants during wound healing. *PLoS One* **9**, e105686, doi:10.1371/journal.pone.0105686 (2014).
62 Specks, U. *et al.* Structure of recombinant N-terminal globule of type VI collagen alpha 3 chain and its binding to heparin and hyaluronan. *EMBO J* **11**, 4281-4290 (1992).
63 Rao, W. H., Hales, J. M. & Camp, R. D. Potent costimulation of effector T lymphocytes by human collagen type I. *J Immunol* **165**, 4935-4940, doi:10.4049/jimmunol.165.9.4935 (2000).
64 Lebbink, R. J. *et al.* Collagens are functional, high affinity ligands for the inhibitory immune receptor LAIR-1. *J Exp Med* **203**, 1419-1425, doi:10.1084/jem.20052554 (2006).
65 Theocharidis, G. *et al.* Type VI Collagen Regulates Dermal Matrix Assembly and Fibroblast Motility. *J Invest Dermatol* **136**, 74-83, doi:10.1038/JID.2015.352 (2016).
66 Castagnaro, S. *et al.* Extracellular Collagen VI Has Prosurvival and Autophagy Instructive Properties in Mouse Fibroblasts. *Front Physiol* **9**, 1129, doi:10.3389/fphys.2018.01129 (2018).
67 DeVorkin, L. *et al.* Autophagy Regulation of Metabolism Is Required for CD8(+) T Cell Anti-tumor Immunity. *Cell Rep* **27**, 502-513 e505, doi:10.1016/j.celrep.2019.03.037 (2019).

68 Botbol, Y., Guerrero-Ros, I. & Macian, F. Key roles of autophagy in regulating T-cell function. *Eur J Immunol* **46**, 1326-1334, doi:10.1002/eji.201545955 (2016).
69 Korolchuk, V. I., Mansilla, A., Menzies, F. M. & Rubinsztein, D. C. Autophagy inhibition compromises degradation of ubiquitin-proteasome pathway substrates. *Mol Cell* **33**, 517-527, doi:10.1016/j.molcel.2009.01.021 (2009).
70 Peng, D. H. *et al.* Collagen promotes anti-PD-1/PD-L1 resistance in cancer through LAIR1-dependent CD8(+) T cell exhaustion. *Nat Commun* **11**, 4520, doi:10.1038/s41467-020-18298-8 (2020).
71 Robertson, C. *et al.* Extracellular matrix modulates T cell clearance of malignant cells in vitro. *Biomaterials* **282**, 121378, doi:10.1016/j.biomaterials.2022.121378 (2022).
72 Lebbink, R. J. *et al.* Mouse leukocyte-associated Ig-like receptor-1 (mLAIR-1) functions as an inhibitory collagen-binding receptor on immune cells. *Int Immunol* **19**, 1011-1019, doi:10.1093/intimm/dxm071 (2007).
73 Meyaard, L. The inhibitory collagen receptor LAIR-1 (CD305). *J Leukoc Biol* **83**, 799-803, doi:10.1189/jlb.0907609 (2008).
74 Jansen, C. A. *et al.* Regulated expression of the inhibitory receptor LAIR-1 on human peripheral T cells during T cell activation and differentiation. *Eur J Immunol* **37**, 914-924, doi:10.1002/eji.200636678 (2007).
75 McLane, L. M., Abdel-Hakeem, M. S. & Wherry, E. J. CD8 T Cell Exhaustion During Chronic Viral Infection and Cancer. *Annu Rev Immunol* **37**, 457-495, doi:10.1146/annurev-immunol-041015-055318 (2019).
76 Metur, S. P. & Klionsky, D. J. Adaptive immunity at the crossroads of autophagy and metabolism. *Cell Mol Immunol* **18**, 1096-1105, doi:10.1038/s41423-021-00662-3 (2021).
77 Pua, H. H., Dzhagalov, I., Chuck, M., Mizushima, N. & He, Y. W. A critical role for the autophagy gene Atg5 in T cell survival and proliferation. *J Exp Med* **204**, 25-31, doi:10.1084/jem.20061303 (2007).
78 Pua, H. H., Guo, J., Komatsu, M. & He, Y. W. Autophagy is essential for mitochondrial clearance in mature T lymphocytes. *J Immunol* **182**, 4046-4055, doi:10.4049/jimmunol.0801143 (2009).
79 Goldblum, J. R. An approach to pleomorphic sarcomas: can we subclassify, and does it matter? *Mod Pathol* **27 Suppl 1**, S39-46, doi:10.1038/modpathol.2013.174 (2014).
80 Sabatelli, P. *et al.* Collagen VI deficiency affects the organization of fibronectin in the extracellular matrix of cultured fibroblasts. *Matrix Biol* **20**, 475-486, doi:10.1016/s0945-053x(01)00160-3 (2001).
81 Bredfeldt, J. S. *et al.* Computational segmentation of collagen fibers from second-harmonic generation images of breast cancer. *J Biomed Opt* **19**, 16007, doi:10.1117/1.JBO.19.1.016007 (2014).
82 Harris, G. M., Raitman, I. & Schwarzbauer, J. E. Cell-derived decellularized extracellular matrices. *Methods Cell Biol* **143**, 97-114, doi:10.1016/bs.mcb.2017.08.007 (2018).
83 Detwiller, K. Y. *et al.* Analysis of hypoxia-related gene expression in sarcomas and effect of hypoxia on RNA interference of vascular endothelial cell growth factor A. *Cancer Res* **65**, 5881-5889, doi:10.1158/0008-5472.CAN-04-4078 (2005).

Acknowledgments:

The authors wish to acknowledge Paolo Bonaldo, Ph.D. for providing WT and Col6-/- MEFs and Rebecca Gladdy, MD, for STS-109 sarcoma cells. In addition, we would like to thank Steven Leppla and his laboratory for *Cmg2*$^{-/-}$cells. We also thank James Hayden and Frederick Keeney of the Wistar Institute Imaging Facility for their assistance with multiphoton microscopy and analysis and John Tobias Ph.D., of the UPenn molecular profiling for facility for bioinformatic assistance. Lastly, we would like to thank Martha Jordan, Ph.D. and Sydney Drury for their assistance with *in vivo* flow cytometry, and Linnea T. Olsson, MSPH, for assistance with molecular epidemiologic analysis of human sarcoma tumors. **Funding:** This work was funded by The University of Pennsylvania Abramson Cancer Center, The Penn Sarcoma Program, Steps to Cure Sarcoma, R01CA229688, U54CA210173, T32HL007971, and the American Cancer Society – Roaring Fork Valley Research Circle Postdoctoral Fellowship (PF-21-111-01-MM).

Author contributions

Conceptualization: JAF, SG, MH, TSKEM

Methodology: JAF, HCP, AMF

Validation: EFW, HCP, HS, YL, AMF, SY, RK, GEC, IM

Formal Analysis: HCP, AMF, RK, GE

Investigation: HCP, AMF, HS, YL, RK, GSE, EFW, SD

Data Curation: MG, YL, AMF

Provision of resources: JAF, SG, MH, TSKEM

Writing-original draft preparation: TSKEM, HCP, AMF

Writing-review and editing: TSKEM, HCP, AMF

Visualization: TSKEM, YL, HCP, AMF, JAF, EFW

Supervision: JAF, SG, MH, TSKEM

Project administration: TSKEM

Funding acquisition: TSKEM, SG

Competing interests: Authors declare no competing interests.

Data and materials availability: Microarray gene expression dataset capturing control and SAHA/JQ1 treated KP cells can be found in the NCBI GEO database with the accession number GSE109923. Microarray gene expression dataset capturing 5 independent KP and 5 independent KPY bulk tumors can be found in the GEO database with the accession number GSE109920. Distribution of Col6-/- MEFs and STS-109 cells is limited by materials transfer agreements (MTAs) with the University of Padua and the University of Toronto Lunenfeld-Tanenbaum, Research Institute respectively. All data and non-MTA protected materials used in the analysis are available to any researcher for purposes of reproducing or extending the analysis. Please contact T.S. Karin Eisinger at karineis@pennmedicine.upenn.edu

Fig. 1. YAP1$^+$ UPS cells inhibit T cell activation and promote CD8$^+$ T cell dysfunction. (**A**) Kaplan-Meier latency curves of LSL-*Kras*$^{G12D+}$; *Trp53*$^{fl/fl}$ (KP); LSL-*Kras*$^{G12D+}$; *Trp53*$^{fl/fl}$; *Yap1*$^{fl/fl}$ (KPY), LSL-*Kras*$^{G12D+}$; *Trp53*$^{fl/fl}$; *Yap1*$^{fl/fl}$; *LSL-Ikk2*$^{CA/A}$ (KPYI), and LSL-*Kras*$^{G12D+}$; *Trp53*$^{fl/fl}$; *Rela*$^{fl/fl}$ (KPR) models of UPS (n >10 per genotype). (**B**) Agarose gel validation of each genotype shown in A. LSL-*Kras*^{G12D}, *Ikk2*^{CA} transgenes are validated by the presence of the indicated band. *Yap1*$^{fl/fl}$ and *Rela*$^{fl/fl}$ alleles are validated by the presence of the corresponding band, and for *Rela*$^{fl/fl}$ animals, absence of wild type bands in a separate reaction with unique PCR primers (data not shown). (**C**) Metascape pathway enrichment analysis of genes identified by microarray of 5 unique bulk KP and KPY tumors. Analysis includes all genes with >2-fold increase in expression in KPY relative to KP. (**D**) Representative contour plots of T cells in KP and KPY tumors harvested 45 and 47 days post-adeno Cre administration, respectively. Events shown are pre-gated on live singlets unless otherwise specified. (**E**) Frequency of CD8$^+$CD44^{hi} and CD4$^+$CD44^{hi} T cells in KP and KPY tumors. Each point represents an individual mouse tumor (n=4 tumors per group); two-tailed unpaired t-test. (**F**) Representative contour plots of CD39, Tim3, and Pd1 expression in CD8$^+$ T cells from KP and KPY tumors. (**G**) Frequency of CD39$^+$Pd1$^+$ and Tim3$^+$Pd1$^+$ effector CD8$^+$ T cells in KP and KPY tumors. Each point represents an individual mouse tumor. Two-tailed unpaired t-test. (**H**) qRT-PCR of bulk KP and KPY tumors; two-tailed unpaired t-test. (**I**) Kaplan Meier survival curves of KP and KPY tumor-bearing mice injected i.p. with α-PD-1 or control compound when tumors became palpable at ~300mm^3. Doses (200 ug i.p.) were given every three days for two weeks. Red and black circles in the control curves indicate IgG-injected and un-injected mice, respectively. Open circle represents a mouse with complete, lasting tumor regression. X-axis represents days since adeno Cre injection. Log-rank test. (**J**) Longitudinal cytolysis of human STS-109 UPS cells expressing shScr or shYAP1 shRNAs following the addition of CART-TnMUC1 cells. Measurements indicate the % cytolysis of target cells (UPS cells). Normalized cell index over time for STS-109 cells alone (not shown) is used to control for differences in target cell growth among groups. Quantification represents the area under the curve (AUC); one-way ANOVA with Dunnett's multiple comparisons test (vs. shSCR). (**K**, **L**) Kaplan Meier survival curves of UPS patients in TCGA-Sarcoma dataset based on *GZMB* (**K**) and *PRF1* (**L**) expression. In (**L**), each tertile (low, medium, high), represents 1/3 of patients. Log-rank test. (**M**, **N**) Correlation of *YAP1* with *GZMB* (**M**) and *PRF1* (**N**) gene expression in UPS tumors from TCGA-Sarcoma dataset.

Fig. 2. UPS-cell intrinsic Yap1 mediates collagen VI (ColVI) deposition in the TME. (**A**) Heat map of gene expression microarray data comparing 5 unique KP and KPY bulk tumors. Map focuses on collagen genes modulated by *Yap1 in vivo* deletion. (FC=fold change). (**B**) Representative images of ColVI IHC in KP and KPY tumor sections. Scale bars for 4X and 20X images = 50 μM. Scale bars for 40X images = 25 μM. (**C**) qRT-PCR validation of *Col6a1*, *Col6a2*, *Col6a3,* and *Yap1* gene expression in KP cells expressing control or one of multiple independent *Yap1*-targeting shRNAs; one-way ANOVA with Dunnett's (vs. shScr), SEM. (**D**) Western blots of KP cells treated as in C. (**E**) Heat map of gene expression microarray data comparing KP cells treated with SAHA (2μM)/JQ1 (0.5μM) or vehicle control for 48 hours. (**F**) Representative images of ColVI IHC in KP tumors from tumor-bearing mice treated with 25mg/kg SAHA+50mg/kg JQ1 or vehicle control for 20 days. (**G**) Western blot of KP cells treated as in E. (**H**) Schematic of experimental model to assess immunomodulatory role of tumor-derived decellularized extracellular matrix (dECM). (**I**) Collagen VI deposition in dECM from KP cells expressing scrambled or *Yap1*-targeting shRNAs. Scale bars=25 μM. (**J**) Representative contour plots and quantification of Pd-1 and Tim3 expression in $CD44^{+}CD8^{+}$ T cells incubated on dECM from control- and shYap1-expressing cells. Each point represents T cells isolated from an individual mouse (n=3 mice per group). Two-tailed unpaired t-test.

Fig. 3. Collagen VI in the UPS TME promotes T cell dysfunction. (**A**) Representative contour plots and (**B**) quantification of Pd1 and Tim3 expression in $CD44^+CD8^+$ T cells incubated on dECM derived from control or shCol6a1 KP cells. Immunofluorescent images of ColVI deposition for each condition are also shown. (**C**) Representative contour plots and (**D**) quantification of Pd-1 and Tim3 expression in $CD44^+CD8^+$ T cells incubated on dECM derived from WT or $Col6a^{-/-}$ mouse embryonic fibroblasts (MEFs). Immunofluorescent images of ColVI deposition for each condition are also shown. (**E**) Longitudinal cytolysis of human STS-109 UPS cells expressing shSCR or shCol6a1 shRNAs following the addition of CART-TnMUC1 cells. Measurements indicate the % cytolysis of target cells. Normalized cell index over time for STS-109 cells alone (not shown) is used to control for differences in target cell growth among groups. (**F**) Quantification of area-under-the-curve (AUC) from E; one-way ANOVA with Dunnett's multiple comparisons test (vs. shScr). (**G**) Tumor growth curves from subcutaneous (flank) syngeneic transplant of 5 x 10^5 KP cells (SKPY42.1 cell line) expressing control or *Col6a1*-targeting shRNAs in C57BL/6 mice. Two-way ANOVA, SEM. (**H**) Visualization of individual tumors from G. Tumor growth curves from G and H are also presented in Fig. 5A. (**I**) Tumor growth curves depicting subcutaneous (flank) syngeneic transplant of 5 x 10^5 KP cells (SKPY42.1 cell line) expressing control or *Col6a1*-targeting shRNAs in C57BL/6 mice treated with α-CD8α every three days. (**J**) Tumor growth curves depicting syngeneic orthotopic transplant (into the gastrocnemius muscle) of 2.5 x 10^5 KP cells (SKPY42.1 cell line) expressing control or *Col6a1*-targeting shRNAs in C57BL/5 mice. Two-way repeated-measures ANOVA, SEM. (**K**) Representative contour plots and (**L**) quantification of T cell dysfunction markers in $CD8^+$ T cells from control and shCol6a1 orthotopic tumors from Fig. 3J. Tumors were generated via syngeneic orthotopic transplant of 2.5 x 10^5 KP cells (SKPY42.1 cell line) into the gastrocnemius muscles of C57BL/6 mice. Each point in K represents individual mouse tumors.

Fig. 4. Collagen I abrogates collagen VI-mediated CD8$^+$ T cell dysfunction (**A**) Representative multiphoton second-harmonic generation (SHG) imaging of KP and KPY tumor sections. All scale bars = 50 μM. (**B, C**) Violin plots of Ct-Fire analysis of SHG tumor images from A. Mean fiber width and linearity were plotted for a minimum 5 separate fields (n≥5 mice per genotype); two-tailed unpaired t-test. (**D**) Representative depth-coded SHG images of human UPS, KP, and KPY explanted live tumors. Red = SHG signal farthest away from the objective/greatest relative depth in the tissue, blue= SHG signal closest to the objective/shallowest relative depth in the tissue. All scale bars = 50 μM. (**E**) Representative ColI IHC staining in KP and KPY tumors. (**F**) Kaplan Meier survival curve of UPS patients in TCGA-Sarcoma dataset based on *LAIR1* gene expression. Each tertile (low, medium, high), represents 1/3 of patients. Log-rank test. (**G-J**) Correlation between *LAIR1* and *YAP1* (**G**), *COL6A3* (**H**), *GZMB* (**I**), and *PRF1* (**J**) gene expression in UPS tumors from TCGA-Sarcoma dataset. Spearman's correlation coefficient was used because data were not normally distributed (Shapiro-Wilk test). (**K**) Schematic of *in vitro* hydrogel system to test the impact of ColI on ColVI-mediated CD8$^+$ T cell dysfunction. CTL = cytotoxic T lymphocyte. (**L-M**) Representative flow cytometry plots (**L**) and quantification (**M**) of activated CD8$^+$CD44$^+$ T cells showing dual expression of TIM3 and PD1 following incubation on hydrogels containing purified COLI with or without purified ColVI. Two-tailed unpaired t-test, SEM. (**N-O**) Representative flow cytometry plots (**N**) and quantification (**O**) of Ki67 positivity in activated CD8$^+$CD44$^+$ T cells incubated on hydrogels containing purified COLI with or without purified COLVI. Two-tailed unpaired t-test, SEM.

Fig. 5. ColVI promotes CD8$^+$ T cell dysfunction by disrupting T cell autophagic flux, which can be restored in the presence of ColI. (**A**) Tumor growth curves from subcutaneous (flank) syngeneic transplant of 5 X10^5 KP cells (SKPY42.1 cell line) expressing control, *Col6a1*, or *Col1a1*-targeting shRNAs in C57BL/6 mice. Two-way ANOVA, SEM. shScr and shCol6a1 tumor growth curves from A are also presented in Fig. 3G, H. (**B**) Kaplan-Meier survival curves of tumors from A. Log-rank test. (**C**) Western blot analysis of KP cells from A-B immediately prior to implantation. (**D**) Tumor growth curves from orthotopic (gastrocnemius muscle) syngeneic transplant of 5 x 10^5 KP cells (SKPY42.1 cell line) expressing control, *Col6a1*, or *Col1a1*-targeting shRNAs in C57BL/6 mice. Two-way ANOVA, SEM. (**E-F**) Visualization (**E**) and quantification (**F**) of autophagosomes in human T cells encapsulated in hydrogels containing purified COLI with or without purified COLVI. Two-tailed unpaired t-test. (**G**) Western blot analysis of LC3B expression in chloroquine-treated human and murine T cells cultured on purified COLI-containing hydrogels in the presence or absence of purified COLVI. (**H-I**) Representative images (**H**) and quantification (**I**) of p62 immunofluorescence in T cells cultured on purified COLI-containing hydrogels with or without purified COLVI.

Fig. 6. YAP1 and COLVI expression/activity are highly correlated in human UPS tumors. (**A**) *COL6A1* gene expression levels in specimens from the Detwiller sarcoma dataset (Oncomine) [83]. DDLS = dedifferentiated liposarcoma, PLS = pleomorphic liposarcoma, FS = fibrosarcoma. (**B**) qRT-PCR analysis of *COL6A1* expression in human sarcoma and normal skeletal muscle tissue specimens (Hospital of the University of Pennsylvania). PLS = pleomorphic liposarcoma, SS = synovial sarcoma, FS = fibrosarcoma. One-way ANOVA with Dunnett's multiple comparisons test (vs. normal skeletal muscle). Normalization was done to *HPRT* expression. (**C-E**) Kaplan-Meier overall survival curves of UPS patients in TCGA-Sarcoma dataset stratified by *COL6A1* (**C**), *COL6A2* (**D**), and *COL6A3* (**E**) gene expression. Each tertile (low, medium, high), represents 1/3 of patients. Log-rank test. (**F**) Correlation of COLVI and nuclear YAP1 immunostaining in UPS tumor specimens (Hospital of the University of Pennsylvania). (**G**) Representative IHC images from F. (**H**) ChIP-seq of *COL6A1*, *COL6A2*, and *COL6A3* promoter H3K27 acetylation in human UPS samples (Hospital of the University of Pennsylvania). (**I-J**) Correlation of *YAP1* with *COL6A3* (**I**) and *FOXM1* (**J**) gene expression in UPS tumors from TCGA-Sarcoma dataset. (**J**). For F, I, and J, Spearman's correlation coefficient was used because data were not normally distributed (Shapiro-Wilk test).

Fig. 7. COLVI expression in the microenvironments of UPS and other soft-tissue sarcoma subtypes. (**A**) Association of IHC-based COLVI expression score with tumor subtype and clinicopathologic features. Sarcoma tissue microarray (TMA). [1]Univariate linear models. [2]In univariate analyses, the Holm-Bonferroni adjustment for multiple comparisons was performed for demographic or clinicopathologic variables with greater than two levels, with $\alpha = 0.05$. Results are considered statistically significant (bold text) if the univariate *P*-value is smaller than the corresponding Holm's alpha. [3]Fully adjusted model (age, grade, stage, and histology). Correction for multiple comparisons was not performed due to insufficient statistical power. [4]Includes 2 alveolar soft part sarcomas, 1 epithelioid hemangioendothelioma, 1 fibroma, 1 glomus tumor, 1 hemangioendothelial sarcoma, 1 hemangiopericytoma, 1 osteosarcoma, and 1 tenosynovial giant cell tumor. [5]Excludes two benign cases. (**B**) Waterfall plot depicting IHC-based COLVI expression scores in individual tumors from A. LMS = leiomyosarcoma; LS = liposarcoma, NL = neurilemmoma, RD = rhabdomyosarcoma, SS = synovial sarcoma, NF = neurofibroma. "Other" as described in A. (**C, D**) Kaplan-Meier disease-free and disease-specific survival curves of (**C**) liposarcoma and (**D**) leiomyosarcoma patients in TCGA-Sarcoma dataset stratified by *COL6A1* gene expression. Each tertile (low, medium, high), represents 1/3 of patients. Log-rank test. (**E**) Model depicting study findings.

Figure 1

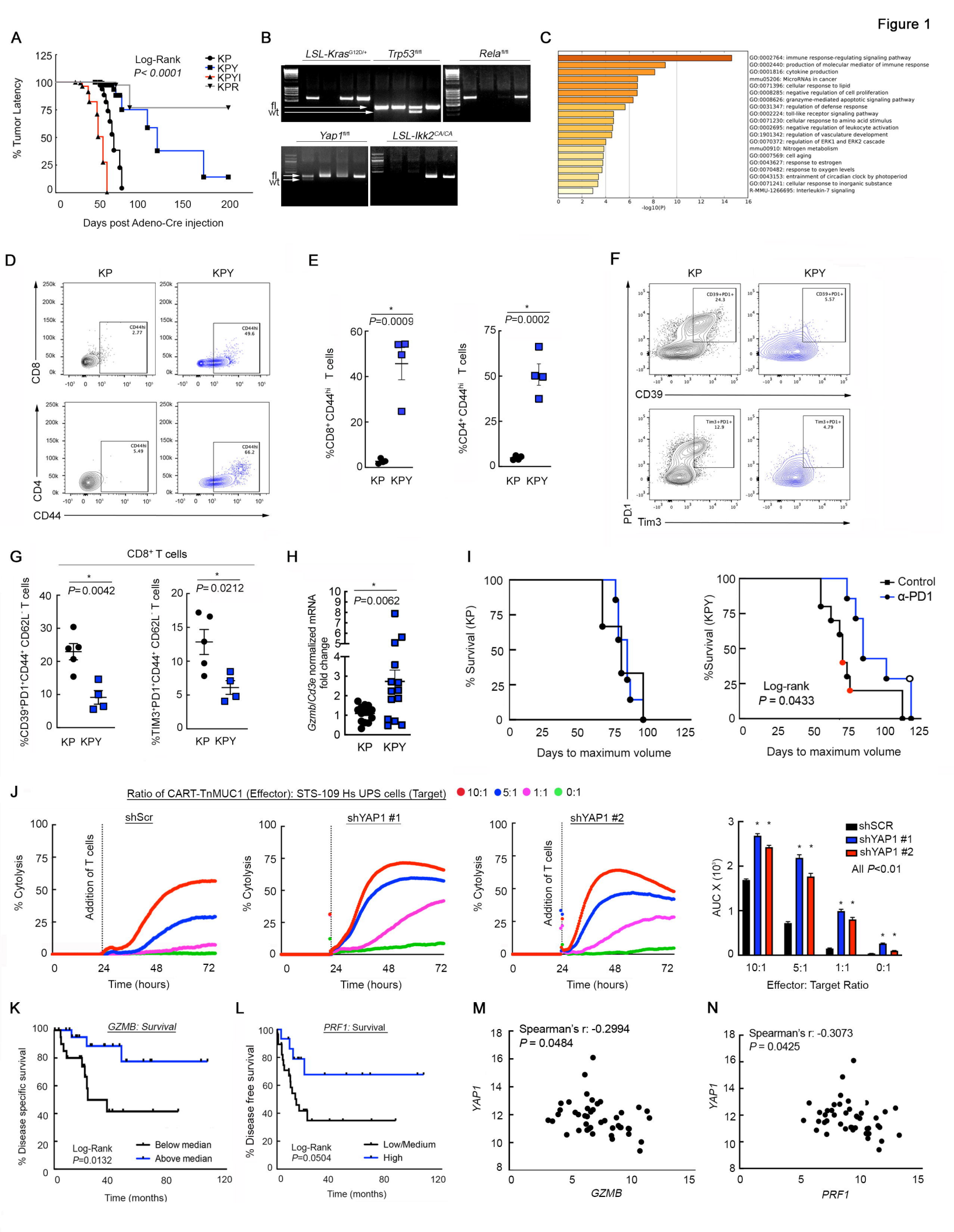
A
Log-Rank
P< 0.0001
KP
KPY
KPYI
KPR
% Tumor Latency
Days post Adeno-Cre injection
B
LSL-Kras G12D/+
Trp53 fl/fl
Rela fl/fl
Yap1 fl/fl
LSL-Ikk2 CA/CA
fl
wt
C
GO:0002764: immune response-regulating signaling pathway
GO:0002440: production of molecular mediator of immune response
GO:0001816: cytokine production
mmu05206: MicroRNAs in cancer
GO:0071396: cellular response to lipid
GO:0008285: negative regulation of cell proliferation
GO:0008626: granzyme-mediated apoptotic signaling pathway
GO:0031347: regulation of defense response
GO:0002224: toll-like receptor signaling pathway
GO:0071230: cellular response to amino acid stimulus
GO:0002695: negative regulation of leukocyte activation
GO:1901342: regulation of vasculature development
GO:0070372: regulation of ERK1 and ERK2 cascade
mmu00910: Nitrogen metabolism
GO:0007569: cell aging
GO:0043627: response to estrogen
GO:0070482: response to oxygen levels
GO:0043153: entrainment of circadian clock by photoperiod
GO:0071241: cellular response to inorganic substance
R-MMU-1266695: Interleukin-7 signaling
-log10(P)
D
KP
KPY
CD8
CD4
CD44
E
P=0.0009
%CD8+ CD44hi T cells
P=0.0002
%CD4+ CD44hi T cells
KP KPY
F
KP
KPY
CD39
PD1
Tim3
G
CD8+ T cells
P=0.0042
%CD39+PD1+CD44+ CD62L- T cells
P=0.0212
%TIM3+PD1+CD44+ CD62L- T cells
KP KPY
H
P=0.0062
Gzmb/Cd3e normalized mRNA fold change
KP KPY
I
% Survival (KP)
Days to maximum volume
Control
α-PD1
%Survival (KPY)
Log-rank
P = 0.0433
Days to maximum volume
J
Ratio of CART-TnMUC1 (Effector): STS-109 Hs UPS cells (Target)
10:1
5:1
1:1
0:1
shScr
shYAP1 #1
shYAP1 #2
% Cytolysis
Addition of T cells
Time (hours)
shSCR
shYAP1 #1
shYAP1 #2
All P<0.01
AUC X (10³)
Effector: Target Ratio
K
GZMB: Survival
% Disease specific survival
Log-Rank
P=0.0132
Below median
Above median
Time (months)
L
PRF1: Survival
% Disease free survival
Log-Rank
P=0.0504
Low/Medium
High
Time (months)
M
Spearman's r: -0.2994
P = 0.0484
YAP1
GZMB
N
Spearman's r: -0.3073
P = 0.0425
YAP1
PRF1

Figure 2

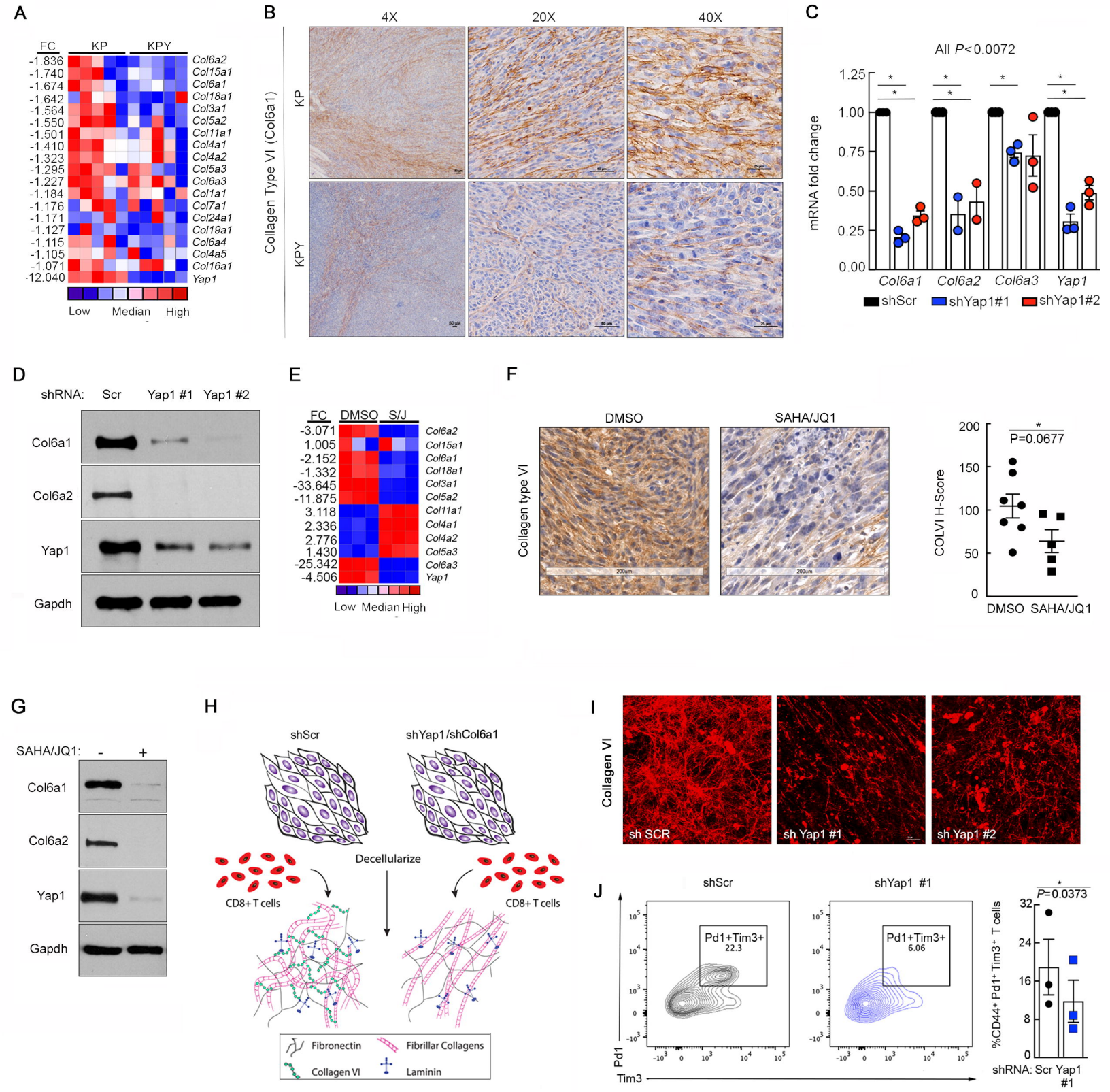
A
FC
KP
KPY
-1.836 Col6a2
-1.740 Col15a1
-1.674 Col6a1
-1.642 Col18a1
-1.564 Col3a1
-1.550 Col5a2
-1.501 Col11a1
-1.410 Col4a1
-1.323 Col4a2
-1.295 Col5a3
-1.227 Col6a3
-1.184 Col1a1
-1.176 Col7a1
-1.171 Col24a1
-1.127 Col19a1
-1.115 Col6a4
-1.105 Col4a5
-1.071 Col16a1
-12.040 Yap1
Low Median High
B
4X
20X
40X
Collagen Type VI (Col6a1)
KP
KPY
C
All P<0.0072
mRNA fold change
1.25
1.00
0.75
0.50
0.25
0.00
Col6a1
Col6a2
Col6a3
Yap1
shScr
shYap1#1
shYap1#2
D
shRNA: Scr Yap1 #1 Yap1 #2
Col6a1
Col6a2
Yap1
Gapdh
E
FC DMSO S/J
-3.071 Col6a2
1.005 Col15a1
-2.152 Col6a1
-1.332 Col18a1
-33.645 Col3a1
-11.875 Col5a2
3.118 Col11a1
2.336 Col4a1
2.776 Col4a2
1.430 Col5a3
-25.342 Col6a3
-4.506 Yap1
Low Median High
F
DMSO
SAHA/JQ1
Collagen type VI
COLVI H-Score
200
150
100
50
0
P=0.0677
DMSO SAHA/JQ1
G
SAHA/JQ1: - +
Col6a1
Col6a2
Yap1
Gapdh
H
shScr
shYap1/shCol6a1
Decellularize
CD8+ T cells
CD8+ T cells
Fibronectin
Fibrillar Collagens
Collagen VI
Laminin
I
Collagen VI
sh SCR
sh Yap1 #1
sh Yap1 #2
J
shScr
shYap1 #1
Pd1+Tim3+
22.3
Pd1+Tim3+
6.06
Pd1
Tim3
%CD44+ Pd1+ Tim3+ T cells
32
24
16
8
0
P=0.0373
shRNA: Scr Yap1 #1

Figure 3

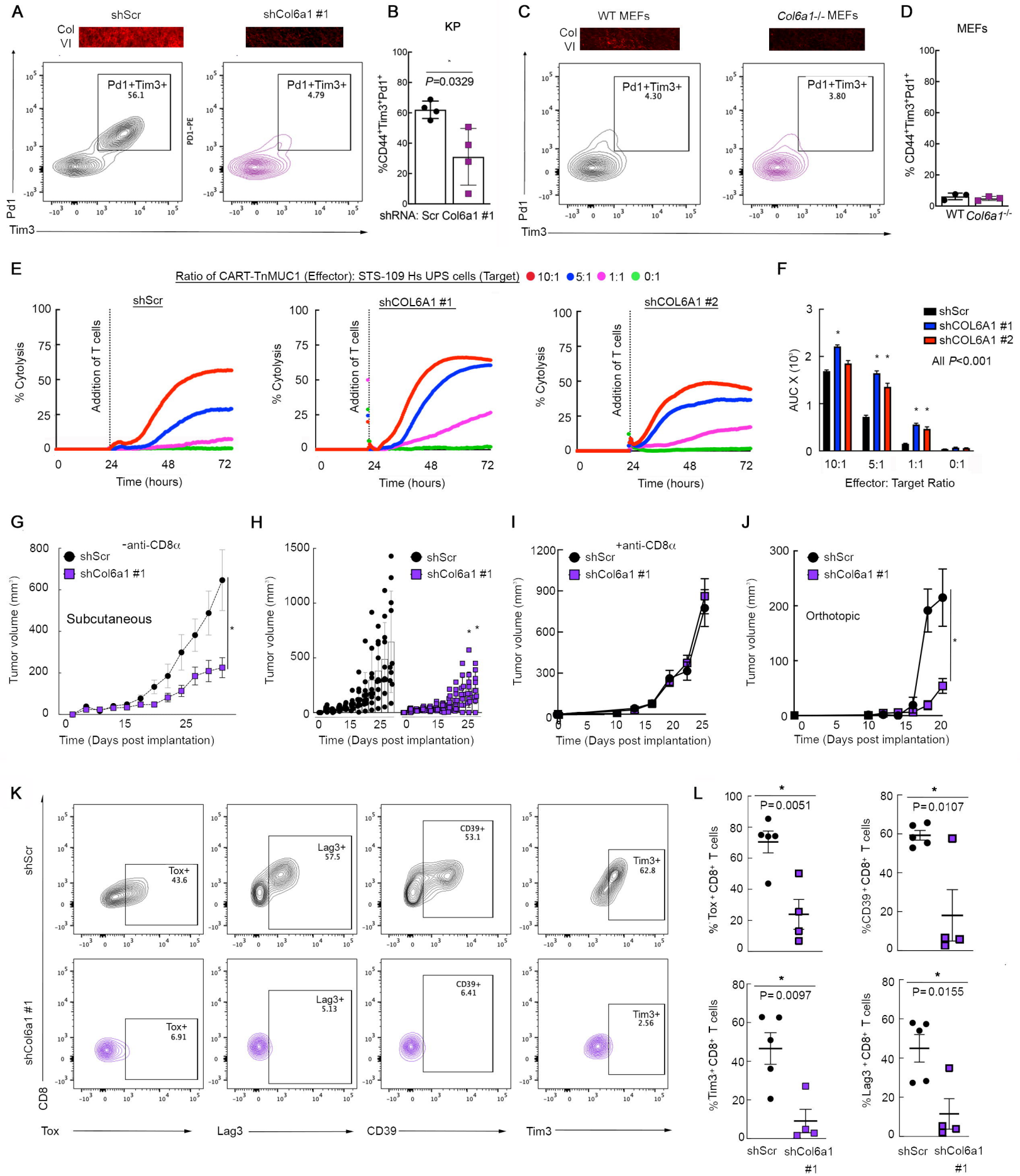
A
shScr
shCol6a1 #1
Col VI
Pd1+Tim3+ 56.1
Pd1+Tim3+ 4.79
Pd1
Tim3
PD1-PE
B
KP
P=0.0329
%CD44+Tim3+Pd1+
shRNA: Scr Col6a1 #1
C
WT MEFs
Col6a1-/- MEFs
Pd1+Tim3+ 4.30
Pd1+Tim3+ 3.80
D
MEFs
% CD44+Tim3+Pd1+
WT Col6a1-/-
E
Ratio of CART-TnMUC1 (Effector): STS-109 Hs UPS cells (Target) 10:1 5:1 1:1 0:1
shScr
shCOL6A1 #1
shCOL6A1 #2
Addition of T cells
% Cytolysis
Time (hours)
F
shScr
shCOL6A1 #1
shCOL6A1 #2
All P<0.001
AUC X (10³)
10:1
5:1
1:1
0:1
Effector: Target Ratio
G
-anti-CD8α
shScr
shCol6a1 #1
Subcutaneous
Tumor volume (mm³)
Time (Days post implantation)
H
shScr
shCol6a1 #1
Tumor volume (mm³)
Time (Days post implantation)
I
+anti-CD8α
shScr
shCol6a1 #1
Tumor volume (mm³)
Time (Days post implantation)
J
shScr
shCol6a1 #1
Orthotopic
Tumor volume (mm³)
Time (Days post implantation)
K
shScr
shCol6a1 #1
CD8
Tox+ 43.6
Lag3+ 57.5
CD39+ 53.1
Tim3+ 62.8
Tox+ 6.91
Lag3+ 5.13
CD39+ 6.41
Tim3+ 2.56
Tox
Lag3
CD39
Tim3
L
P=0.0051
% Tox+CD8+ T cells
P=0.0107
%CD39+CD8+ T cells
P=0.0097
% Tim3+CD8+ T cells
P=0.0155
%Lag3+CD8+ T cells
shScr
shCol6a1 #1

Figure 4

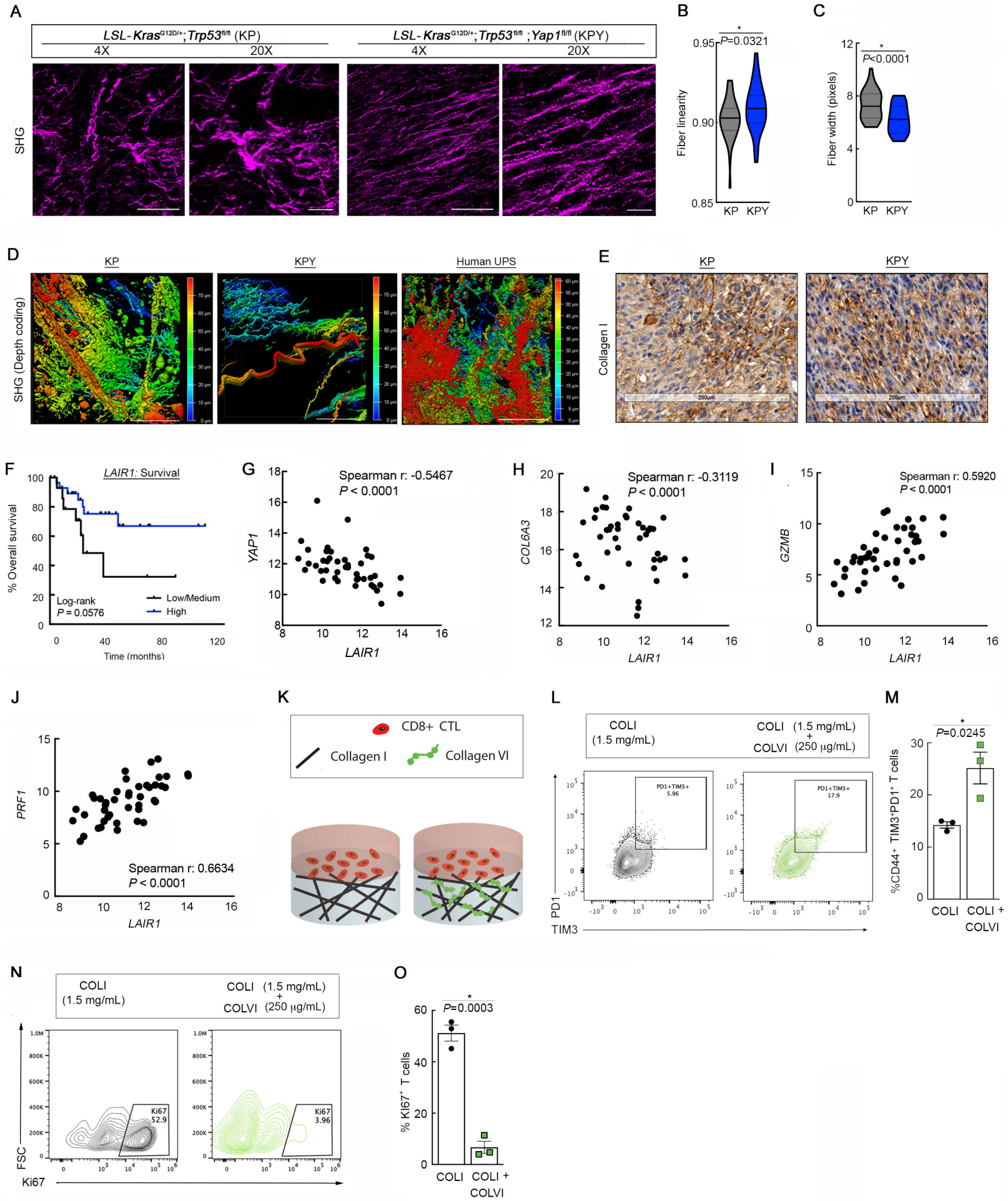
A
LSL-KrasG12D/+;Trp53fl/fl (KP)
LSL-KrasG12D/+;Trp53fl/fl;Yap1fl/fl (KPY)
4X
20X
SHG
B
P=0.0321
Fiber linearity
KP
KPY
C
P<0.0001
Fiber width (pixels)
D
KP
KPY
Human UPS
SHG (Depth coding)
E
Collagen I
F
LAIR1: Survival
% Overall survival
Log-rank
P = 0.0576
Low/Medium
High
Time (months)
G
Spearman r: -0.5467
P < 0.0001
YAP1
LAIR1
H
Spearman r: -0.3119
P < 0.0001
COL6A3
I
Spearman r: 0.5920
P < 0.0001
GZMB
J
PRF1
Spearman r: 0.6634
P < 0.0001
K
CD8+ CTL
Collagen I
Collagen VI
L
COLI (1.5 mg/mL)
COLI (1.5 mg/mL) + COLVI (250 µg/mL)
PD1+TIM3+ 5.96
PD1+TIM3+ 17.9
PD1
TIM3
M
P=0.0245
%CD44+ TIM3+PD1+ T cells
COLI
COLI + COLVI
N
COLI (1.5 mg/mL)
COLI (1.5 mg/mL) + COLVI (250 µg/mL)
Ki67 52.9
Ki67 3.96
FSC
Ki67
O
P=0.0003
% Ki67+ T cells
COLI
COLI + COLVI

Figure 5

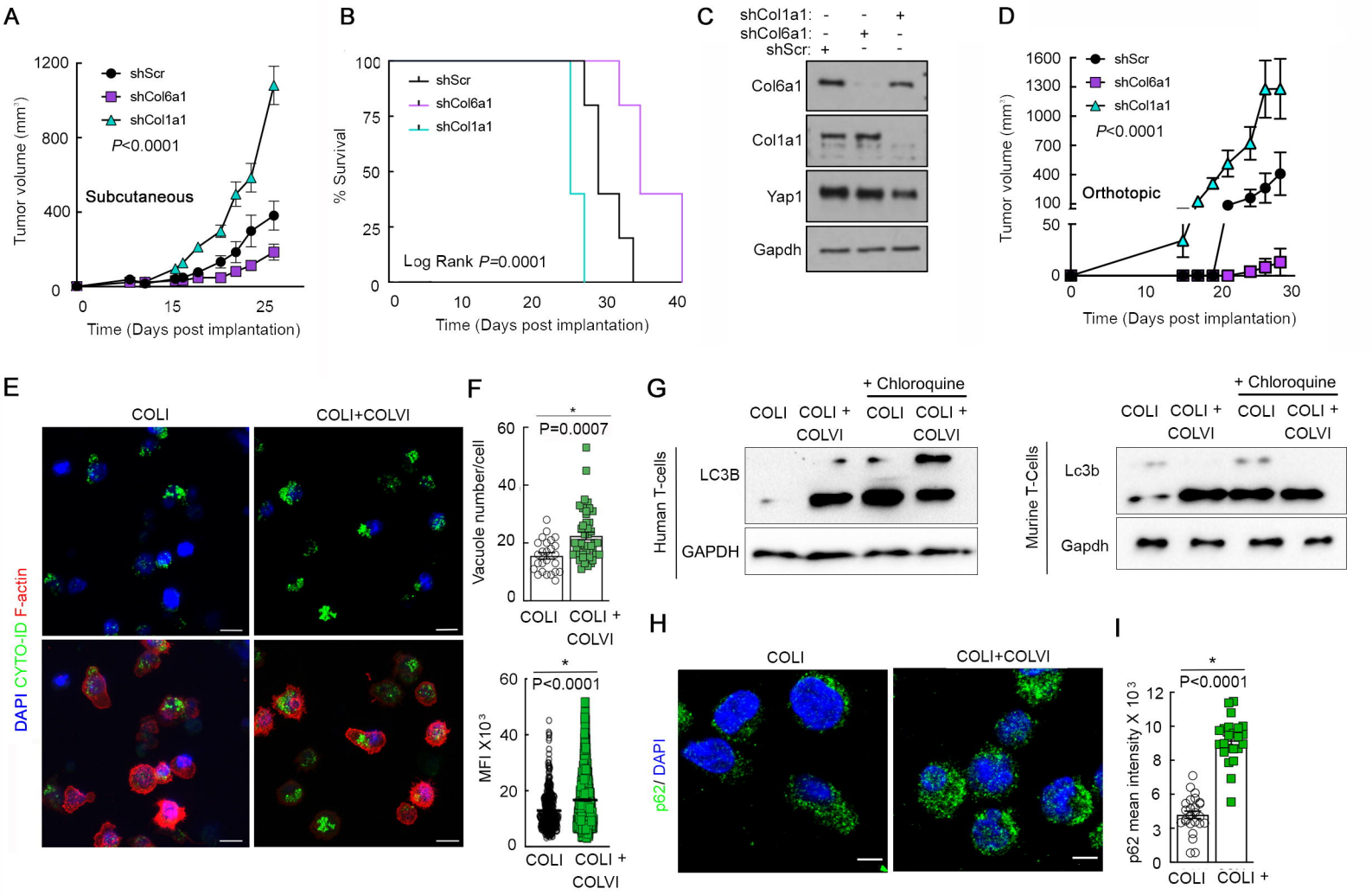
A
shScr
shCol6a1
shCol1a1
P<0.0001
Subcutaneous
Tumor volume (mm³)
Time (Days post implantation)
B
shScr
shCol6a1
shCol1a1
Log Rank P=0.0001
% Survival
Time (Days post implantation)
C
shCol1a1:
shCol6a1:
shScr:
Col6a1
Col1a1
Yap1
Gapdh
D
shScr
shCol6a1
shCol1a1
P<0.0001
Orthotopic
Tumor volume (mm³)
Time (Days post implantation)
E
COLI
COLI+COLVI
DAPI CYTO-ID F-actin
F
P=0.0007
Vacuole number/cell
COLI
COLI + COLVI
P<0.0001
MFI X10³
G
+ Chloroquine
COLI
COLI + COLVI
Human T-cells
LC3B
GAPDH
Murine T-Cells
Lc3b
Gapdh
H
COLI
COLI+COLVI
p62/ DAPI
I
P<0.0001
p62 mean intensity X 10³
COLI
COLI +

Figure 6

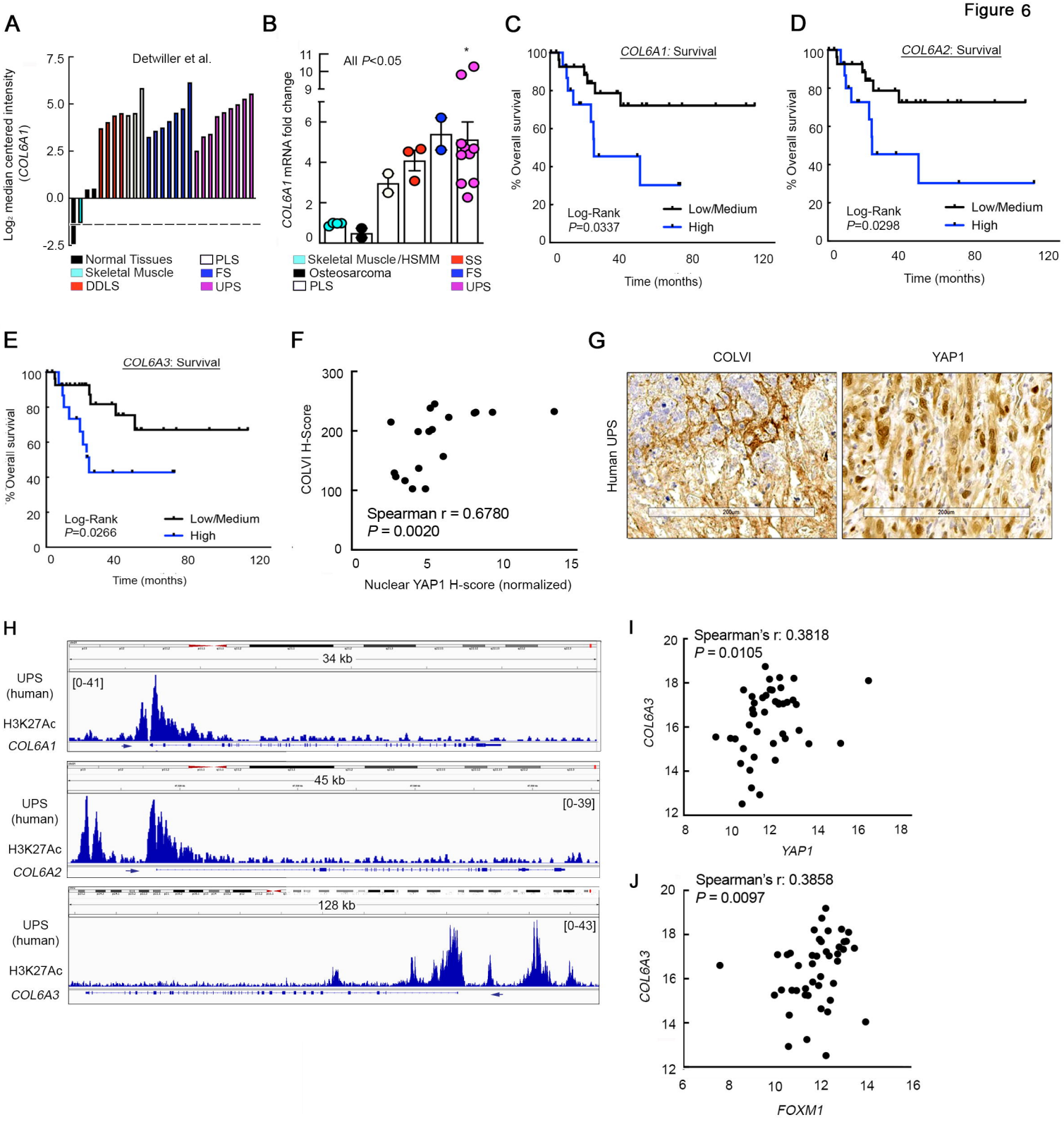
A
Detwiller et al.
Log2 median centered intensity (COL6A1)
7.5
5.0
2.5
0.0
-2.5
Normal Tissues
Skeletal Muscle
DDLS
PLS
FS
UPS
B
All P<0.05
COL6A1 mRNA fold change
Skeletal Muscle/HSMM
Osteosarcoma
PLS
SS
FS
UPS
C
COL6A1: Survival
% Overall survival
Log-Rank P=0.0337
Low/Medium
High
Time (months)
D
COL6A2: Survival
% Overall survival
Log-Rank P=0.0298
Low/Medium
High
Time (months)
E
COL6A3: Survival
% Overall survival
Log-Rank P=0.0266
Low/Medium
High
Time (months)
F
COLVI H-Score
Spearman r = 0.6780
P = 0.0020
Nuclear YAP1 H-score (normalized)
G
COLVI
YAP1
Human UPS
H
34 kb
UPS (human)
[0-41]
H3K27Ac
COL6A1
45 kb
UPS (human)
[0-39]
H3K27Ac
COL6A2
128 kb
UPS (human)
[0-43]
H3K27Ac
COL6A3
I
Spearman's r: 0.3818
P = 0.0105
COL6A3
YAP1
J
Spearman's r: 0.3858
P = 0.0097
COL6A3
FOXM1

A

Table 1: COLVI expression score: associations with patient characteristics and tumor clinicopathologic features

		n (%)	Mean H-score (95% CI)	*P-value*[1]	Holm's α[2]	*P-* adj.[3]
Histology						
	UPS (REF.)	11 (15.71)	88.52 (17.99)			
	Leiomyosarcoma	9 (12.86)	42.89 (9.78)	**0.0003**	0.0071	0.0089
	Liposarcoma	17 (24.29)	87.69 (11.58)	0.9360	0.0500	0.9777
	Neurilemmoma	12 (17.14)	60.69 (18.90)	0.0140	0.0125	0.0765
	Neurofibroma	3 (4.29)	30.83 (15.85)	**0.0013**	0.0083	0.0097
	Other[4]	9 (12.86)	60.86 (19.37)	0.0228	0.0167	0.1070
	Rhabdomyosarcoma	5 (7.14)	81.17 (21.46)	0.6072	0.0250	0.7430
	Synovial sarcoma	4 (5.71)	38.88 (11.69)	**0.0020**	0.0100	0.0031
Age (y)						
	> 50 (REF.)	36 (51.43)	69.89 (10.67)			
	≤ 50	34 (48.57)	66.60 (10.46)	0.6687	N/A	0.8950
Grade[5]						
	G1-G2 (REF.)	30 (44.12)	55.51 (9.36)			
	G3-G4	38 (55.88)	77.87 (10.32)	0.0013	N/A	0.0197
Stage[5]						
	I (REF.)	18 (26.47)	60.64 (12.26)			
	II	18 (26.47)	67.62 (15.54)	0.5115	0.05	0.2414
	III	32 (47.06)	74.66 (11.51)	0.1385	0.025	0.1093

B

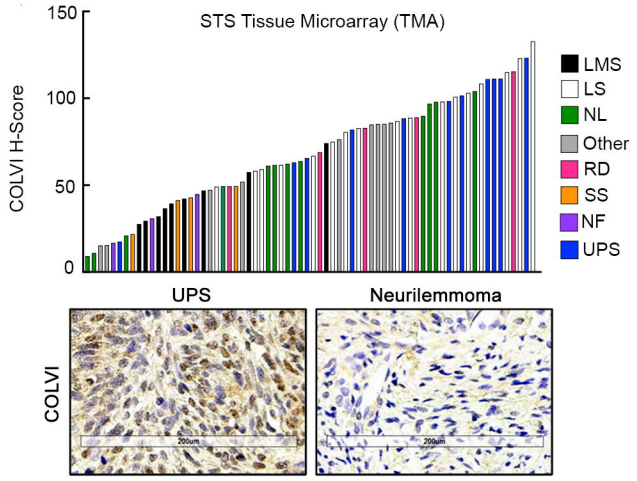

C

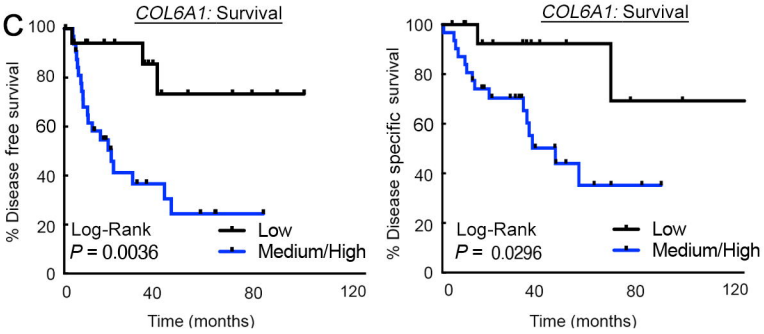

Liposarcoma

D

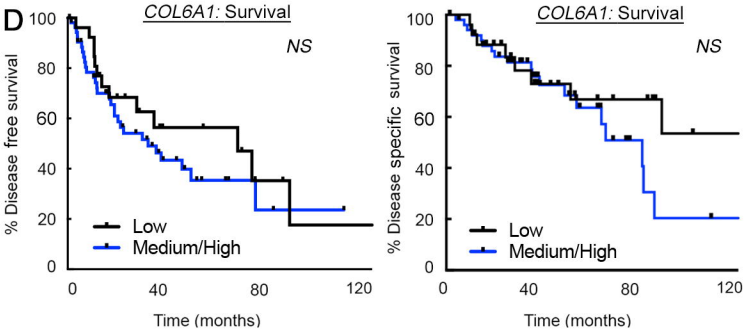

Leiomyosarcoma
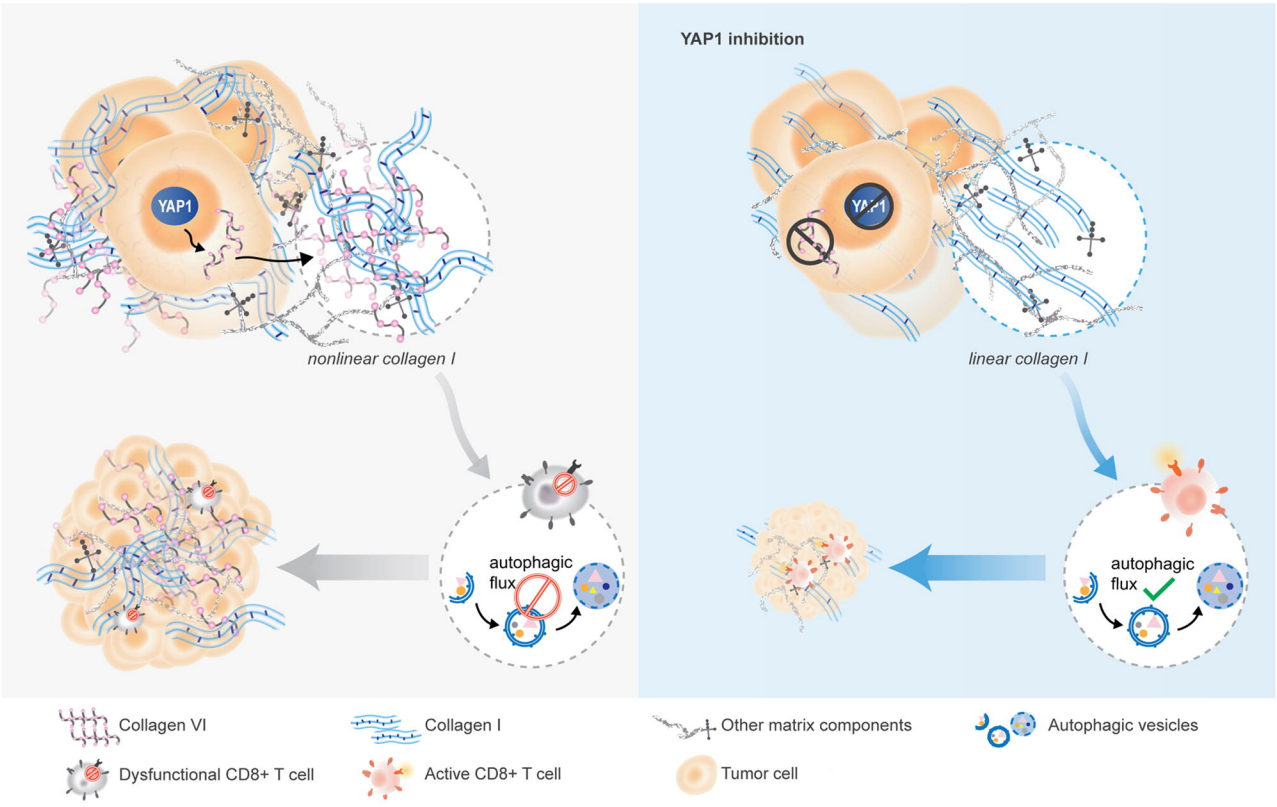
E